Patient-derived mutations impact pathogenicity of SARS-CoV-2

Hangping Yao[1]†, Xiangyun Lu[1]†, Qiong Chen[2]†, Kaijin Xu[1], Yu Chen[1], Linfang Cheng[1], Fumin Liu[1], Zhigang Wu[1], Haibo Wu[1], Changzhong Jin[1], Min Zheng[1]*, Nanping Wu[1]*, Chao Jiang[2,3]*, Lanjuan Li[1]*

[1]State Key Laboratory for Diagnosis and Treatment of Infectious Diseases, National Clinical Research Center for Infectious Diseases, First Affiliated Hospital, Zhejiang University School of Medicine, Hangzhou, China.

[2]Life Sciences Institute, Zhejiang University, Hangzhou, China.

[3]Zhejiang Provincial Key Laboratory of Pancreatic Disease, First Affiliated Hospital, Zhejiang University School of Medicine, Hangzhou, China.

†Equal contributions.

*Corresponding authors: M.Z. (minzheng@zju.edu.cn), N.W. (flwnp2013@163.com), C.J. (jiang_chao@zju.edu.cn), and L.L. (ljli@zju.edu.cn).

Summary (130 words)

The sudden outbreak of the severe acute respiratory syndrome–coronavirus (SARS-CoV-2) has spread globally with more than 1,300,000 patients diagnosed and a death toll of 70,000. Current genomic survey data suggest that single nucleotide variants (SNVs) are abundant. However, no mutation has been directly linked with functional changes in viral pathogenicity. We report functional characterizations of 11 patient-derived viral isolates. We observed diverse mutations in these viral isolates, including 6 different mutations in the spike glycoprotein (S protein), and 2 of which are different SNVs that led to the same missense mutation. Importantly, these viral isolates show significant variation in cytopathic effects and viral load, up to 270-fold differences, when infecting Vero-E6 cells. Therefore, we provide direct evidence that the SARS-CoV-2 has acquired mutations capable of substantially changing its pathogenicity.

Introduction

Severe acute respiratory syndrome coronavirus 2 (SARS-CoV-2; previously referred to as 2019-nCoV), associated with the ongoing outbreak of atypical pneumonia, has already caused a global pandemic beginning in Wuhan, Central China, despite China's extensive

35 systematic effort to contain the outbreak. As of April 7, 2020, SARS-CoV-2 has infected
36 more than 1.3 million people around the world with a death toll of 70,000. The numbers
37 are still increasing rapidly. The estimate of the incubation period of SARS-CoV-2 (mean,
38 5.1 days; range, 4.5 to 5.8 days) (Lauer et al., 2020) is in line with those of other known
39 human coronaviruses, such as SARS (mean, 5 days; range, 2 to 14 days) (Varia et al.,
40 2003) and MERS (mean, 5 to 7 days; range, 2 to 14 days) (Virlogeux et al., 2016). The
41 reproductive number of SARS-CoV-2 is likely to be from 1.4 to 6.5, with a mean of 3.3
42 (Liu et al., 2020), which is slightly higher than SARS, i.e., 2-5 (Bauch et al., 2005;
43 Lipsitch et al., 2003) and MERS, i.e., 2.7-3.9 (Lin et al., 2018). More than half of patients
44 with SARS-CoV-2 showed no signs of fever before hospitalization (Guan et al., 2020).
45 Strikingly, Coronavirus Diease-2019 (COVID-19) can be transmitted by asymptomatic
46 patients, who show no fever, gastrointestinal or respiratory symptoms, and have normal
47 chest computed tomography (Bai et al., 2020; Hu et al., 2020), making it much more
48 challenging to prevent the spread of COVID-19. Moreover, SARS-CoV-2 can remain
49 viable and infectious in aerosols for multiple hours and up to 7 days on surfaces (van
50 Doremalen et al., 2020). Although multiple *in vitro* studies or clinical trials on inhibitors
51 or drugs were carried out, no effective cures or vaccines have been found so far (Cao et

52 al., 2020; Hoffmann et al., 2020; Wang et al., 2020). The World Health Organization
53 (WHO) declared COVID-19 a Public Health Emergency of International Concern on 30
54 January 2020, and raised the threat of the SARS-CoV-2 pandemic to the "very high"
55 level on February 28, 2020.

56 SARS-CoV-2 is the seventh member of enveloped RNA beta-coronavirus
57 (Sarbecovirus subgenus) (Zhu et al., 2020); SARS-CoV-2, SARS-CoV and MERS-CoV
58 can lead to devastating diseases, while HKU1, NL63, OC43 and 229E are related with
59 mild symptoms (Corman et al., 2018). So far, no recombination events were detected (Yu,
60 2020), although this could be at least partially due to the fact that most viral isolates were
61 sequenced with short-reads platform. The transmembrane spike (S) glycoprotein mediates
62 viral entry into host cells through homotrimers protruding from the viral surface. The S
63 protein includes two domains: S1 for binding to the host cell receptor and S2 for fusion of
64 the viral and cellular membranes, respectively (Tortorici and Veesler, 2019). Both
65 SARS-CoV-2 and SARS-CoV use the angiotensin converting enzyme 2 (ACE2) to enter
66 target cells (Walls et al., 2020). ACE2 is expressed in human nasal epithelial cells and
67 lung, spermatogonia, leydig, sertoli, gastric, duodenal, and rectal epithelial cells (Wang
68 and Xu, 2020; Xiao et al., 2020; Zhao et al., 2020). The receptor binding domain (RBD)

69 in the S protein is the most variable genomic part in the betacoronavirus group (Wu et al.,
70 2020; Zhou et al., 2020), and some sites of S protein might be subjected to positive
71 selection (Lv et al., 2020). Despite the abundant variability of SARS-CoV-2, one key
72 question remains as to whether these mutations have any real functional impact on the
73 pathogenicity of SARS-CoV-2. This is crucial in our understanding of the viral infectious
74 mechanisms and dictates the strategy of drug and vaccine development in preparation for
75 the next stage of the pandemic.

76 To address this, we characterized 11 SARS-CoV-2 viral isolates from patients
77 admitted to Zhejiang University-affiliated hospitals in Hangzhou, China, situated 757
78 KMs to the east of Wuhan (see Materials and Methods). Super-deep sequencing of the 11
79 viral isolates on the Novaseq 6000 platform identified 1-5 mutations in the coding
80 sequences among the viral isolates. Mixed viral populations (representing quasi-species)
81 were also observed. We infected Vero-E6 cells with 11 viral isolates and quantitatively
82 assessed their viral load at 1, 2, 4, 8, 24, and 48 hours post infection (P.I.) and their viral
83 cytopathic effects (CPE) at 48 and 72 hours P.I.. Our results show that the observed
84 mutations can have a direct impact on the viral load and CPE when infecting Vero-E6
85 cells, as much as 270-fold differences between the extremities. This finding suggests that

86 the observed mutations in our study, and possibly in the viral isolates collected around
87 the world, can significantly impact the pathogenicity of SARS-CoV-2.
88
89 **Results**
90 **Summary of the epidemiological history of the patients**
91 The samples of the 11 patients involved in this study were collected during the early
92 phase of the COVID-19 breakout in China, dates ranging from 1/22/2020 to 2/4/2020
93 (Table 1). 10 of the 11 patients had clear connections with Wuhan city, where the
94 SARS-CoV-2 was originally identified. 5 of the 11 people either worked in or traveled to
95 Wuhan before they were diagnosed, and another 5 had close contact with people who
96 lived in Wuhan, and the remaining person had contact with people who were COVID-19
97 victims. Notably, patients ZJU-4, -5, -9 attended the same business conference where a
98 few colleagues from Wuhan were present. These patients therefore constitute 1st and 2nd
99 generations of the viral victims based on their epidemiological history. The 11 patients
100 include 8 males and 3 females, with ages ranging from 4 months to 71 years old. There
101 are no clear criteria in selecting these patients other than the fact that they were all
102 admitted into Zhejiang University-affiliated hospitals in Hangzhou. All except one of the

103 patients had moderate or worse symptoms. 3 patients had co-morbidity conditions and

104 one patient needed ICU treatment. Luckily, all of the patients have recovered as of the

105 time of writing this article.

ID	Sex	Age	Sample	Sample collection date	Virus isolating date	Epide-miology	Viral gen	Onset sypmtoms	Severity	Blood presure	ICU	Onset date	Admission	Discharge
ZJU_1	M	36	Sputum	1.25	1.29	Contact with people from Wuhan	2	Fever	Moderate	0	0	1.23	1.25	2.23
ZJU_2	M	31	Sputum	1.26	1.29	Lived in Wuhan	1	Fever	Severe	0	0	1.23	1.24	2.23
ZJU_3	M	32	Sputum	1.25	1.30	Traveled to Wuhan	2	Fever	Severe	0	0	1.18	1.19	2.12
ZJU_4	M	34	Sputum	1.24	1.28	Conference with colleagues from Wuhan	2	Fever, fatigue	Moderate	0	0	1.17	1.21	2.9
ZJU_5	F	25	Sputum	1.22	1.26	Conference with colleagues from Wuhan	2	Fever	Severe	0	0	1.21	1.22	2.9
ZJU_6	M	71	Sputum	2.2	2.6	Contact with people who had COVID19 Wuhan.	2 or 3	Fever, fatigue	Severe	1	0	1.22	1.26	2.19
ZJU_7	F	4M	Nasopharyngeal swab	2.3	2.8	Contact with people from Wuhan	2	Fever	Mild	0	0	1.29	1.29	2.20
ZJU_8	M	53	Sputum	1.26	1.30	Lived in Wuhan	1	Fever, fatigue	Critical	1	1	1.17	1.22	2.19
ZJU_9	M	30	Stool	1.28	2.7	Conference with colleagues from Wuhan	2	Fever	Severe	0	0	1.18	1.21	2.5
ZJU_10	F	38	Stool	2.3	2.8	Lived in Wuhan	1	Fever	Severe	0	0	1.19	1.27	2.12
ZJU_11	M	62	Stool	2.4	2.9	Lived in Wuhan	1	Coughing	Severe	1	0	1.19	1.26	3.15

106

107 **Table 1.** A summary of the epidemiological information of the 11 patients involved in

108 this study. The "Viral gen" (viral generation) was inferred based on their exposure

109 history.

110

111 **Ultra-deep sequencing reveals diverse mutations in the patient-derived viral isolates**

112 To assess the mutational spectrum of these 11 viral isolates, ultra-deep sequencing of the

113 isolated viral genomic RNA was performed on the Illumina Novaseq 6000 platform,

114 generating on average 245 million post-cleaning reads/67.16 Gb per sample (Table S1;
115 average coverage exceeding 2,000,000 X). This extraordinary depth is partially due to the
116 small genome of the SARS-CoV-2, which enables us to identify mutations with high
117 confidence. Moreover, in cases where the viral populations are not homogenous, the
118 depth could help us to characterize alleles with very low frequency.

119 In total, 33 mutations were identified (including 10 mutations observed in
120 mixed-populations), and 19 of these mutations were novel, according to the comparison
121 with 1111 genomic sequences available at GISAID on 3/24/2020 (Fig. 1, S1, and S2).
122 Specifically, G11083T and G26144T were found in ZJU-1, and both of these mutations
123 are known as founding mutations for a large group of viruses (Capobianchi et al., 2020).
124 C8782T and T28144C were found in two of our viral isolates, ZJU-2 and ZJU-8, and
125 these two are known as the founding mutations for another large group of viral isolates
126 (Capobianchi et al., 2020). Interestingly, mutation T22303G was found in five viral
127 isolates (ZJU-2, -5, -9, -10, and -11) and ZJU-5 and ZJU-9 were exposed to the same
128 potential source of infection during a business conference (Table 1). Previously, only one
129 viral isolate identified in Australia had the T22303G mutation. Strikingly, the viral isolate
130 from patient ZJU-4, who attended the same conference as ZJU-5 and ZJU-9, has a novel

131 mutation, A22301C, which causes the same missense mutation at the protein level
132 (S247R in the S protein) as T22303G, mutating the 1st instead of the 3rd position in the
133 respective codon. Observations of these two single nucleotide variants can only be
134 coincidental, albeit very unexpected. Finally, the ZJU-11 has 4 mutations in the ORF7b
135 gene, 3 of which are consecutive and introduce 2 mutations at the protein level.
136 Di-nucleotide and Tri-nucleotide mutations are of course rarer than SNV, but not
137 exponentially so, according to previous mutational accumulation studies in prokaryotes
138 (Lynch, 2007).

139 It is important to note that while the sequence data deposited in GISAID are very
140 helpful in tracking inter-personal variation of the virus, we still do not know much about
141 intra-personal viral evolutionary dynamics. For example, in ZJU-4 and ZJU-10, alleles of
142 two separate sites have very similar frequency distributions, indicating that these two
143 sites are probably linked, representing at least two haplotypes within the viral populations.
144 And as revealed by this study, 6 of the identified mutations would have been ignored if
145 using the consensus sequences for analyses. Taken together, despite only 11
146 patient-derived isolates being analyzed in this study, we observed abundant mutational
147 diversity, including several founding mutations for different major clusters of viruses

now circulating globally. This diverse mutational spectrum is consistent with their relatively early sampling time and relative proximity to Wuhan city, where the first viral strain was identified. The full mutational diversity of the virus in Wuhan city in the early days is still unknown to this day, due to limited sampling (Lu et al., 2020; Zhou et al., 2020).

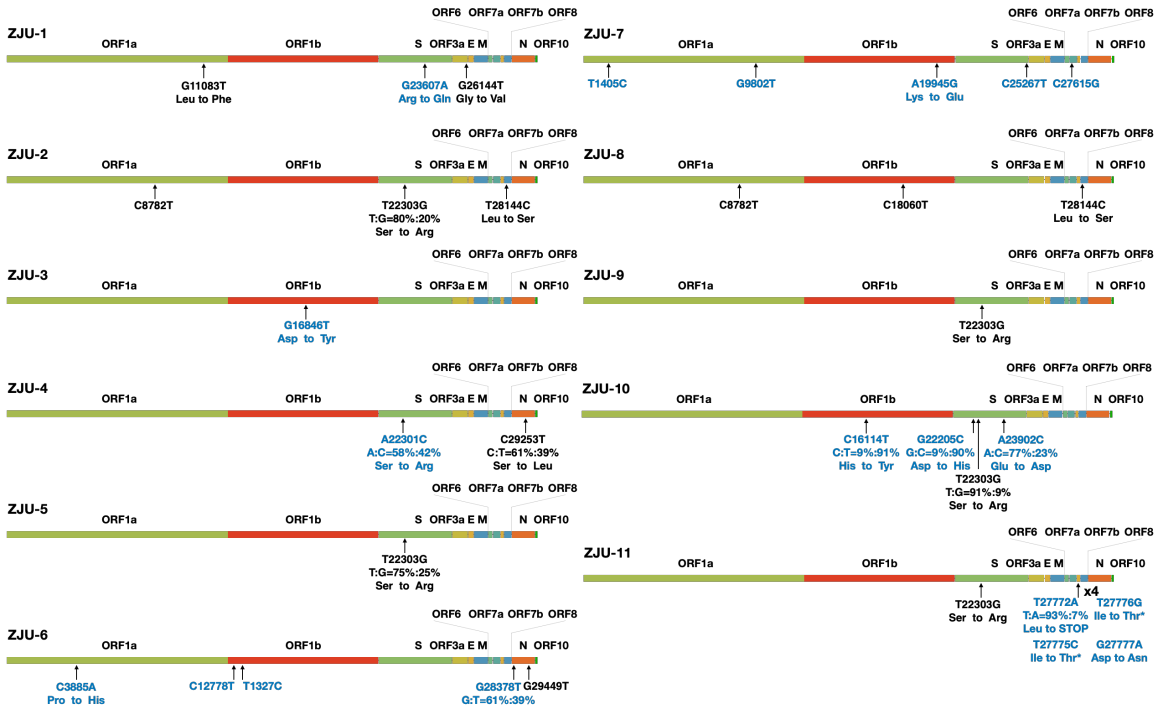

Fig. 1. A summary of the mutations identified in each of the 11 viral isolates. Each ORF of the viral genome was denoted based on the annotations of NC_045512.2 as provided by NCBI. If a mutation was observed in the context of a mixed population, the respective percentages of the top two alleles are provided. Changes at the amino acid level are provided if applicable. Blue color indicates novel mutation at the time of writing the

159 article.

160

161 **Phylogenetic analysis of the patient-derived viral isolates reveals their diverse**

162 **evolutionary history**

163 To understand the phylogenetic context of 11 viral isolates with respect to the corpus of

164 available SARS-CoV-2 sequencing data, we acquired 725 high quality and high coverage

165 SARS-CoV-2 genomes from GISAID (downloaded on 3/21/2020), including the Yunnan

166 RaTG13 viral strain and the Guangdong pangolin viral strain as the outgroup. We aligned

167 the 736 genomic sequences with MAFFT (see Materials and Methods) and trimmed the

168 full-length alignment with trimAL (see Materials and Methods) to remove any spurious

169 parts of the alignment. We used iqtree (see Materials and Methods) to construct a

170 1000-times bootstrapped maximum-likelihood phylogenic tree of the 736 viral sequences

171 based on 835 parsimony informative sites (Fig. 2A). The resulting phylogenetic tree is

172 largely consistent with the phylogenetic analysis being updated on GISAID (Fig. S3). We

173 want to emphasize that due to the rapidly developing COVID-19 situation, tens or even

174 hundreds of new sequences are being uploaded to the GISAID every day. As a result,

175 new observations may be generated when more data are available.

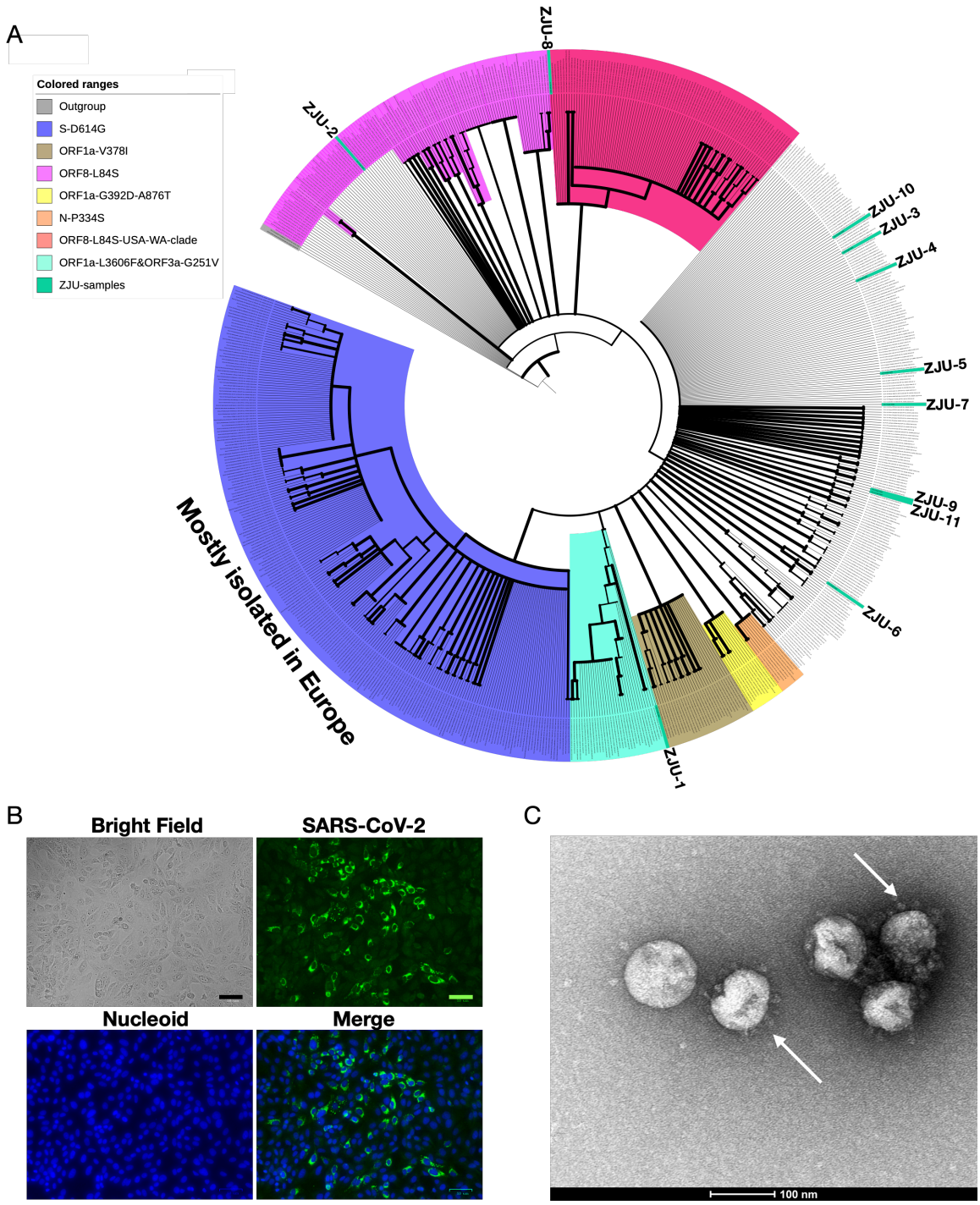

Fig. 2. Characterizations of the patient-derived SARS-CoV-2 isolates. (A) Phylogenetic analyses of the 11 viral isolates in the context of 725 SARS-CoV-2 sequences

179 downloaded from GISAID. The 1000-times bootstrapped maximum likelihood tree was
180 constructed to demonstrate the phylogenetic context of the 11 viral isolates. Major and
181 minor clusters were color-coded and denoted as shown in the "colored ranges" inset box.
182 All ZJU- samples were color-codded as green. The width of a branch indicates bootstrap
183 supporting level. (B) Fluorescent labeling of the viral S protein indicates that isolated
184 SAR-CoV-2 viral particles (Green) bind to the peripherals of the Vero-E6 cells (DNA
185 stained as Blue) prior to entry. Scale bars, 50 μm. (C) A representative TEM picture of
186 the isolated SAR-CoV-2 viral particles, arrows indicate the iconic "crown" consisted of S
187 proteins (Spike). Scale bar, 100 nm.

188

189 We observed quite a few sets of founding mutations. Specifically, we note the
190 following three biggest clusters in our phylogenetic analysis: 1. Three nucleotide
191 mutations C241T (silent), C14408T (silent), and A23403G (D614G in S) found a group
192 of 231 viral sequences (Fig. 2A; S-D614G cluster), most of which were isolated in
193 Europe; 2. Two nucleotide mutations C8782T (silent) and T28144C (L84S in ORF8),
194 found a group of 208 viral sequences (Fig. 2A; ORF8-L84S cluster), which is not

195 monophyletic in our analysis (Fig. 2A and S3). However, a distinct monophyletic
196 subclade of 92 sequences within the ORF8-L84S cluster can be observed, mainly
197 composed of viral sequences isolated from Seattle, USA (Fig. 2A;
198 ORF8-L84S-USA-WA-clade); 3. Two nucleotide mutations, G11083T (L3606F in
199 ORF1a), and G26144T (G251V in ORF3a) found a group of 34 viral sequences, most of
200 which were from Netherlands and England. Several smaller monophyletic clusters,
201 defined by different sets of founding mutations (bootstrap supporting value >95), can be
202 observed. For examples: 1. the G1937A (V378I in ORF1a) mutation founds a cluster of
203 31 viral sequences; 2. the G1440A and G2891A mutations, resulting in G392D and
204 A876T mutations in the ORF1a gene, founds a cluster of 12 viral sequences, mostly from
205 Germany or Netherlands; 3. the C15325T and C29303T mutations, resulting in P344S
206 mutation in the N gene, founds a small cluster of 8 sequences, all of which are from
207 China or Japan. When integrating the characterized 11 viral isolates into the phylogenetic
208 analysis, they are dispersed across the entire phylogenetic space. ZJU-1 clusters with the
209 ORF1a-L3606F & ORF3a-G251V groups, as it has both of the two defining mutations
210 (Fig. 2A). ZJU-2 and ZJU-8, on the other hand, cluster with the ORF8-L84S cluster
211 because they both have the two founding mutations (Fig. 2A). ZJU-9 and ZJU-11 cluster

212 with an Australian isolate because of the aforementioned T22303G mutation. The rest of
213 the group either have few mutations or novel mutations that do not cluster with any
214 known sizable groups, reflecting the extensive diversity within our 11 samples. Taken
215 together, some monophyletic clusters of viruses do show obvious geographic patterns
216 (Europe and WA-USA especially), but this could be due to the founding effect of
217 respective mutations that happened early during the initial phase of the pandemic.
218

219 **Patient-derived SARS-CoV-2 isolates show significant variation in viral copy**
220 **number and cytopathic effects when infecting Vero-E6 cells**

221 There is much speculations and many theories behind the observed mutations in
222 sequenced viral isolates. Theoretically, one usually needs not often invoke selection
223 arguments in explaining the origin of these mutations, as the human to human infection
224 process is a series of repeated naturally-occurring bottlenecking events, in which the
225 seeding viral population can be as little as hundreds of viral copies (Forni et al., 2017).
226 Therefore, a significant portion of the genetic diversity or even population-specific
227 fixations could be due to this process, where selection plays a small role (Renzette et al.,
228 2017). We conducted Tajima's test of neutrality using the constructed alignment of viral

229 sequences and Taijima's D is -2.8874 with a nucleotide diversity (π) of 0.000641 ($p <$
230 0.05 according to simulations performed in (Tajima, 1989), indicating that the
231 SARS-CoV-2 genome has an excess of low-frequency alleles due to recent population
232 expansions, consistent with the repeated bottlenecking events during viral infections.
233 However, certain mutations do provide selection advantages or disadvantages under
234 specific circumstances, as shown by the discovery that adaptive mutations are highly
235 enriched in the interface between the S protein and the human ACE2 receptor (Ou et al.,
236 2020).

237 To examine the mutational impact of the patient-derived SARS-CoV-2 isolates, we
238 conducted *in vitro* infectivity assay. We chose *in vitro* assay because COVID-19 patients
239 show a wide variety of clinical symptoms ranging from asymptotic to death, and
240 epidemiological research have shown that the clinical outcomes are heavily influenced by
241 individual's age, complications, and other potential unknown parameters (Guan et al.,
242 2020). We first examined whether the viral isolates could successfully bind to Vero-E6
243 cells as expected (Fig. 2B), and visually identified the viral particles with the iconic
244 "crown" formed by S proteins (Fig. 2C and S4A). We then infect the Vero-E6 cells with
245 all 11 patient-derived viral isolates and harvest the cells at 1, 2, 4, 8 (in quadruplicates),

246 24, and 48 (in duplicates) hours P.I. (see Materials and Methods); we included the
247 supernatant because cell death releases viral particles. DIC micrographs of the cells at 48
248 hours and 72 hours P.I. were also taken to assess the CPE. We used specific real-time
249 reverse transcriptase–polymerase chain reaction (RT-PCR) targeting ORF1a, E, and N
250 genes to detect the presence of SARS-CoV-2 (see Materials and Methods). Cycle
251 threshold values, C_t, were used to quantify the viral load, with lower values indicating
252 higher viral load. Because the results based on the three genes are highly consistent ($R >$
253 0.99, $p < 2.2e-16$), we will only discuss the results of the ORF1a gene (Fig. 3A). We
254 failed to detect any significant signals from our negative controls, hence we simply
255 assigned a C_t value of 40 for all them.

256 Briefly, the C_t values of samples remained mostly flat with small fluctuations for all
257 of the viral isolates at 1, 2, and 4 hours P.I. (Fig. 3A and B). During these early hours,
258 viral particles are binding to gain access into the cells, and replications would rarely
259 occur (Schneider et al., 2012). At 8 hours P.I., we observed significant decreases in Ct
260 value (increases in viral load) for ZJU-6, ZJU-7, ZJU-9, ZJU-10, and ZJU-11. At 24
261 hours P.I., we observed significant decreases in C_t values for all of the viral isolates
262 except for ZJU-2 and ZJU-7, although some of the viral isolates, namely ZJU-10 and

263 ZJU-11, decreased much faster than the others (Fig. 3A and B). At 48 hours P.I., we
264 observed small decreases for all viral isolates except for ZJU-10 and ZJU-11, both of
265 which had presumably already plateaued at 24 hours P.I. (Fig. 3A and B). Notably, at 24
266 hours P.I., ZJU-2 and ZJU-8, members of the ORF-8-L84S cluster (majority of USA
267 WA-Seattle isolates are in this group), showed considerably lower viral loads (Fig. 4A).
268 On the other hand, ZJU-1, which clusters with the S-D614G clade (mostly found in
269 Europe), has a viral load 19 times ($2^{4.25}$) higher than ZJU-2 and ZJU-8 (Fig. 4A). In
270 addition, a near 270-fold difference ($2^{8.09}$) in viral load was observed between ZJU-10
271 and ZJU-2 at 24 hours P.I. (Fig. 4A). These differences became statistically significant at
272 48 hours P.I., and are reproducible when analyzing data on gene E and N (Fig. S4B and C;
273 Fig. S5A). Therefore, different viral isolates, which are defined by different mutations in
274 their genomes, exhibit a significant variation of viral load when infecting Vero-E6 cells.
275 We next examined whether a higher viral load leads to more cell death (Fig. 4B).
276 When examining these cell lines under a microscope at 48 hours and 72 hours P.I., the
277 CPE, or the cell death rate, are highly consistent with the viral load data (Fig. 4C and S5B,
278 C, and D; at 48 hours P.I., C_t vs CPE, $R = -0.72$, $p = 0.015$), indicating that a higher viral
279 load leads to a higher cell death ratio. Note that the C_t numbers are negatively correlated

with the CPE because a lower C_t number means a higher viral load.

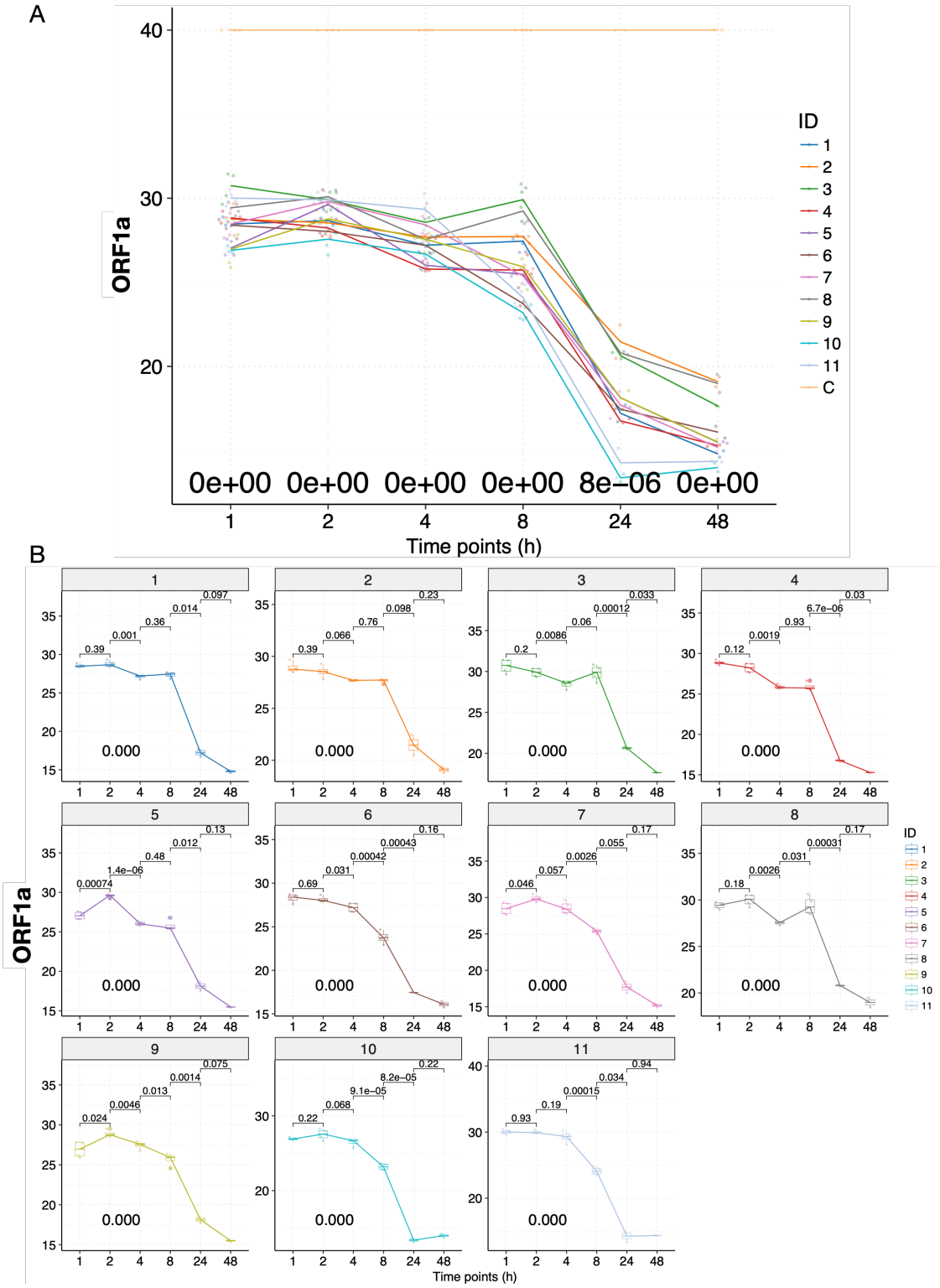

282 **Fig. 3.** The infectivity assay reveals temporal variation in the viral load of the
283 patient-derived SARS-CoV-2 isolates when infecting Vero-E6 cells. (A) Time-series
284 plots of the C_t values (corresponding to the multiplicative inverse of viral load) of the
285 SAR-CoV-2 ORF1a gene over the course of infectivity assay. Each viral isolate plus the
286 negative control "C" was color-coded accordingly. P-values were calculated using the
287 ANOVA method to compare the means of all 11 viral isolates at each time point,
288 excluding the negative control "C". (B) Time-series plots of the C_t values of the
289 SAR-CoV-2 ORF1a gene for each of the 11 patient-derived viral isolates. P-values were
290 calculated between consecutive time points using the t-test and adjusted p-values are
291 shown.
292

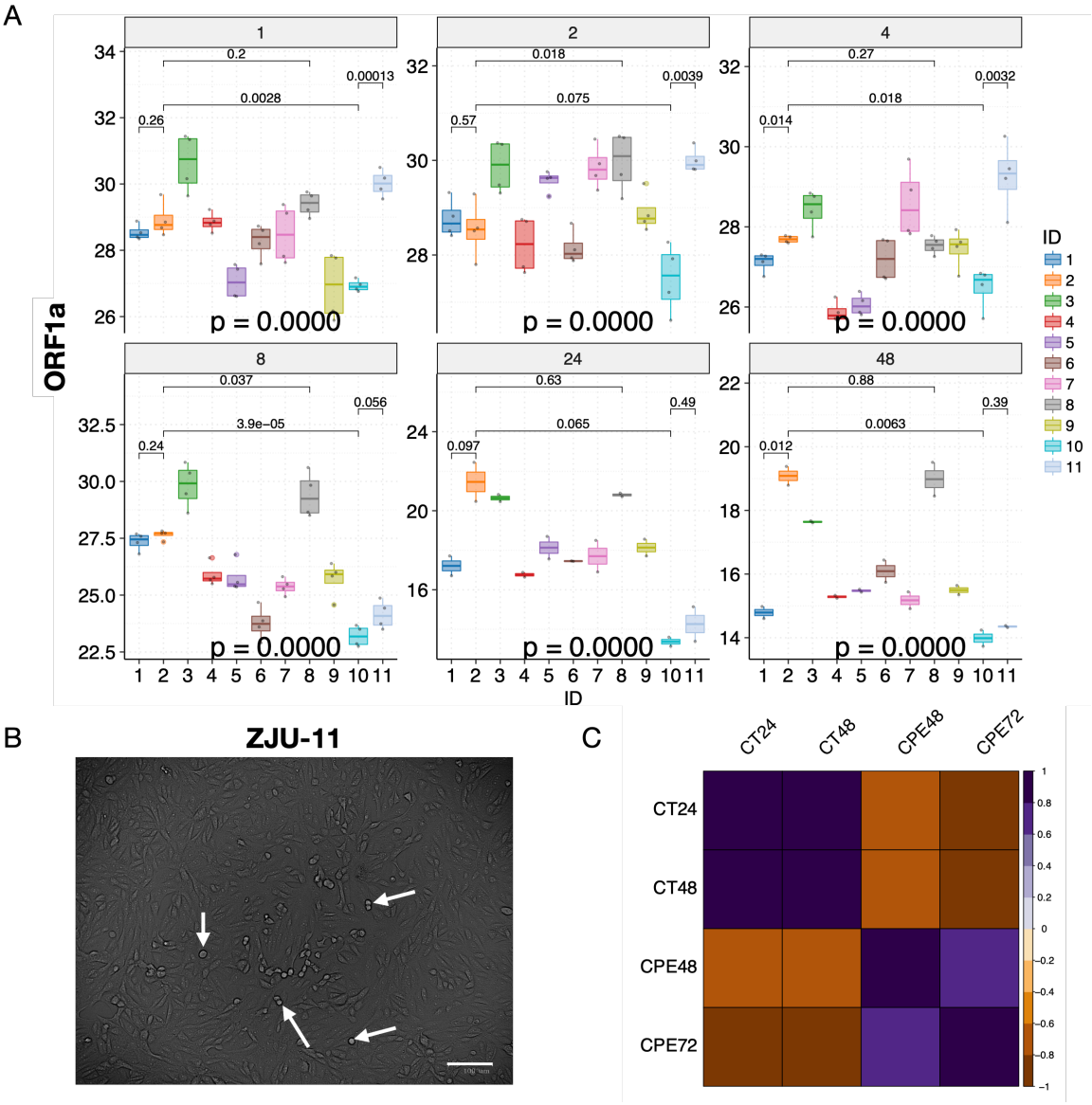

293

294 **Fig. 4.** The changes in CPE and viral load are highly correlated. (A) Significant

295 variations in viral load were observed at each time point. Mean C_t values of selected viral

296 isolates are displayed and color-coded, respectively. P-values were calculated using the

297 ANOVA method to compare the means of all 11 viral isolates at each time point.

298 Pair-wise p-values were calculated between isolates using the t-test and adjusted p-values

299 are shown. (B) Cytopathic effects were visible under the microscope 48 hours P.I., white
300 arrows indicate representative cells undergoing lysis. (C) Cytopathic effects (CPE) were
301 highly correlated with viral load (CT) in viral infectivity assay. Pearson correlations were
302 calculated and p-values were adjusted accordingly; only correlations with adjusted
303 p-value < 0.05 are shown. Note that the CT values are negatively correlated with CPE
304 values because CT values represent the inverse number of viral loads.
305

306 **Discussion**

307 The quickly-developing COVID-19 pandemic has already infected millions of victims
308 and caused 70,000 deaths globally. While many ongoing research projects are attempting
309 to track the evolutionary origin of the virus, find the mechanisms of infection, and
310 produce vaccines or drugs against the virus, we sought to establish the
311 genotype-phenotype link behind the abundant diversity being observed as a result of
312 global sequencing efforts (GISAID). Due to the extremely wide variety of clinical
313 symptoms shown in the patients, establishing a genotype-phenotype link in patients
314 would be very difficult. The *in vitro* cell line provides an ideal system to examine the
315 mutational impact of different isolates of viruses, when all other confounding factors are

316 removed. Although the Vero-E6 cell line was not derived from human, the ACE2 protein
317 of the Vero-E6 cell line is highly similar to that of Human (Fig. S6) and we provided
318 direct evidence that the SARS-CoV-2 can infect the cell line (Fig. 2B).

319 Several findings stand out in our study: 1. A diverse collection of mutations was
320 identified in the 11 viral isolates, including two sets of founding mutations for two major
321 clusters of viruses currently infecting the world population. In addition, 19 of the 31
322 identified mutations are novel, despite the relatively early sampling dates, indicating that
323 the true diversity of the viral strains is still largely underappreciated; 2. remarkably, the
324 T22303G and A22301C mutations result in the same S247R mutation in the S protein
325 (Fig. 1 and S1), mapping to the existing structure revealed that this residue is located in a
326 flexible loop region within the N-terminal domain of the S1 subunit of S protein,
327 although the exact position of S247 could not be determined (Fig. S7, red arch). While
328 the N-terminal domain is not directly involved with binding to ACE2 (Walls et al., 2020)
329 we note that this domain is positioned right next to the C-terminal domain, which binds to
330 ACE2. Interestingly, the T22303G mutation was observed in 5 viral isolates, albeit in
331 different proportions, indicating that this specific mutation was already present in the
332 early days of pandemic, and probably in a significant number of people of Wuhan,

333 despite the fact that it is still largely missing from current GISAID collection. This could
334 be due to the founding effect of mutations, in which case the T22303G mutation was not
335 transmitted out of the China during the early days; 3. The tri-nucleotide mutation in
336 ZJU-11 is unexpected; we note that this specific viral isolate is quite potent in our viral
337 load and CPE assay, and its patient remained positive for an astounding period of 45 days
338 and was only recently discharged from the hospital (Table 1). Investigating the functional
339 impact of this tri-nucleotide mutation would be highly interesting. We note that in the
340 current database, another trinucleotide mutation (G28881A, G2882A and G28883C) has
341 been identified, which also results in two missense mutations at the protein level (Fig. S8).
342 It leads to a cluster of more than 300 viral strains as of the time of writing this article, and
343 its mutational impact on the viral pathogenicity would be worth investigating. Finally, in
344 contrary to the recent report that a viable viral isolate could not be obtained from stool
345 samples, three of our viral isolated were extracted from stool samples, indicating that the
346 SARS-CoV-2 is capable of replicating in stool samples (Woelfel et al., 2020).

347 In short, our study provides direct evidence that mutations currently occurring in the
348 SARS-CoV-2 genome have the functional potential to impact the viral pathogenicity.
349 Therefore, viral surveillance should be also performed at the cellular level when possible,

350 in addition to the accumulating genomic sequencing data. Furthermore, characterizations
351 of all founding mutations in the major geo-based clusters of viruses could be very useful
352 in helping determining if there are actionable pathogenicity differences to aid the current
353 battle against the virus. Finally, similar to flu, drug and vaccine development, while
354 urgent, need to take the impact of these accumulating mutations, especially the founding
355 mutations, into account to avoid potential pitfalls.

356

357 **Figure legends**

358 **Table 1.** A summary of the epidemiological information of the 11 patients involved in
359 this study. The "Viral gen" (viral generation) was inferred based on their exposure
360 history.

361 **Fig. 1.** A summary of the mutations identified in each of the 11 viral isolates. Each ORF
362 of the viral genome was denoted based on the annotations of NC_045512.2 as provided
363 by NCBI. If a mutation was observed in the context of a mixed population, the respective
364 percentages of the top two alleles are provided. Changes at the amino acid level are
365 provided if applicable. Blue color indicates novel mutation at the time of writing the
366 article.

367 **Fig. 2.** Characterizations of the patient-derived SARS-CoV-2 isolates. (A) Phylogenetic
368 analyses of the 11 viral isolates in the context of 725 SARS-CoV-2 sequences
369 downloaded from GISAID. The 1000-times bootstrapped maximum likelihood tree was
370 constructed to demonstrate the phylogenetic context of the 11 viral isolates. Major and
371 minor clusters were color-coded and denoted as shown in the "colored ranges" inset box.
372 All ZJU- samples were color-codded as green. The width of a branch indicates bootstrap
373 supporting level. (B) Fluorescent labeling of the viral S protein indicates that isolated
374 SAR-CoV-2 viral particles (Green) bind to the peripherals of the Vero-E6 cells (DNA
375 stained as Blue) prior to entry. Scale bars, 50 μm. (C) A representative TEM picture of
376 the isolated SAR-CoV-2 viral particles, arrows indicate the iconic "crown" consisted of S
377 proteins (Spike). Scale bar, 100 nm.

378 **Fig. 3.** The infectivity assay reveals temporal variation in the viral load of the
379 patient-derived SARS-CoV-2 isolates when infecting Vero-E6 cells. (A) Time-series
380 plots of the C_t values (corresponding to the multiplicative inverse of viral load) of the
381 SAR-CoV-2 ORF1a gene over the course of infectivity assay. Each viral isolate plus the
382 negative control "C" was color-coded accordingly. P-values were calculated using the

383 ANOVA method to compare the means of all 11 viral isolates at each time point,
384 excluding the negative control "C". (B) Time-series plots of the C_t values of the
385 SAR-CoV-2 ORF1a gene for each of the 11 patient-derived viral isolates. P-values were
386 calculated between consecutive time points using the t-test and adjusted p-values are
387 shown.

388 **Fig. 4.** The changes in CPE and viral load are highly correlated. (A) Significant
389 variations in viral load were observed at each time point. Mean C_t values of selected viral
390 isolates are displayed and color-coded, respectively. P-values were calculated using the
391 ANOVA method to compare the means of all 11 viral isolates at each time point.
392 Pair-wise p-values were calculated between isolates using the t-test and adjusted p-values
393 are shown. (B) Cytopathic effects were visible under the microscope 48 hours P.I., white
394 arrows indicate representative cells undergoing lysis. (C) Cytopathic effects (CPE) were
395 highly correlated with viral load (CT) in viral infectivity assay. Pearson correlations were
396 calculated and p-values were adjusted accordingly; only correlations with adjusted
397 p-value < 0.05 are shown. Note that the CT values are negatively correlated with CPE
398 values because CT values represent the inverse number of viral loads.

399

400

401 # STAR Methods

402 ## Experimental Model and Subject Details

403 Patients with confirmed COVID-19 were admitted in the First Affiliated Hospital from
404 Jan 19 to Mar 5, 2020. The First Affiliated Hospital, located in Hangzhou, Zhejiang
405 Province, China, is one of the major provincial hospitals designated to receive patients
406 with COVID-19 infection across the Zhejiang Province; therefore, patients with severe
407 symptoms outside of Hangzhou were also admitted. Starting Jan 10, 2020, all patients
408 presenting to the hospital's fever clinic were screened by clinical staff for COVID-19
409 infection utilizing criteria for suspected cases as defined by the National Health
410 Commission of China's clinical diagnosis and management guideline for COVID-19
411 (China National Health Committee, 2020). Briefly, patients were screened based on their
412 clinical symptoms and their risk of epidemiological exposure, including past travel to
413 Hubei Province or close contact with people who had visited Hubei Province during the
414 COVID-19 outbreak. As the pandemic continued to spread, the probability of
415 transmission outside of Hubei Province increased. The epidemiological exposure to
416 Hubei Province was not a prerequisite for suspected cases. All suspected cases were
417 determined by laboratory tests and based on positive results of qRT-PCR assay for
418 COVID-19. Patients were excluded if two qRT-PCR tests 24 hours apart both suggested

419 negative results. Patients' clinical samples which PCR test C_t value less than 28 were
420 collected to isolate SARS-Cov-2.

421

422 ## Method Details

423 **Sample collection, Viral isolation, cell infection, and electron microscopy**

424 All samples, sources including sputum, nasopharyngeal swab, and stool, were collected
425 from patients with COVID-19 with consent from all patients. The study was approved by
426 the Clinical Research Ethics Committee of The First Affiliated Hospital, School of
427 Medicine, Zhejiang University (Approval notice 2020-29) for emerging infectious
428 diseases. All collected samples were sent to BSL-3 lab for viral isolation within 4 hours.

429 The sputum, stool, and nasopharyngeal swab samples were pre-processed by first
430 mixing with appropriate volume (Sputum, 5-10 volumes; Stool, 2 ml/100 mg;
431 Nasopharyngeal swab, 1 volume) of MEM medium with 2% FBS, Amphotericin B (100
432 ng/ml), Penicillin G (200 units/ml), Streptomycin (200 μg/ml), and TPCK-trypsin (4
433 μg/ml). The supernatant was collected after centrifugation at 3000 rpm at room
434 temperature. Before infecting Vero-E6 cells, all collected supernatant was filtered using a
435 0.45 μm filter to remove cell debris etc.

436 For viral infection and isolation, 3 ml of filtered supernatant was added to Vero-E6
437 cells in a T25 culture flask. After incubation at 35°C for 2h to allow binding, the
438 inoculum was removed and replaced with fresh culture medium. The cells were incubated
439 at 35°C and observed daily to evaluate cytopathic effects (CPE). The supernatant was

440 tested for SARS-CoV-2 by qRT-PCR (see below for qRT-PCR protocol). Once the
441 qRT-PCR test shows positive (typically after 4-5 days of incubation), the viral particles
442 were collected from culture supernatant by ultra-speed centrifugation (100,000x g for 2
443 hours) for downstream sequencing, infectivity assay, and were observed under 200 kV
444 Tecnai G2 electron microscope.
445
446 **Immunofluorescence staining**
447 Vero-E6 Cells were infected by SARS-CoV-2 for 24 hours, and then fixed in 80%
448 acetone (chilled at -20°C) at room temperature for 10 min. The cells were washed three
449 times with ice-cold PBS, blocked with 1% BSA for 30 min, and incubated with
450 SARS-CoV-2 Spike rabbit monoclonal antibody (dilution ratio 1:200) at room
451 temperature for 1 hour. The cells were again washed three times in ice-cold PBS, and
452 then stained with the Alexa Fluor488®-conjugated Goat Anti-rabbit IgG secondary
453 antibody (Abcam, Cat No. ab150077) for 1 hour at room temperature in the dark. The
454 cells were washed three times and then incubated in 0.5 μg/mL DAPI (nuclear DNA stain)
455 for 5 min. Immunofluorescence was detected and picture were taken using the IX81
456 Olympus microscope equipped with a fluorescence apparatus.
457
458 **Viral infectivity assay**
459 Vero-E6 cells were grown in a 24-well plate and infected with different SARS-CoV-2
460 isolates in duplicates at MOI of 0.5. The inoculum was removed at 1 hours P.I. for the
461 1-hour timepoint group and at 2 hours P.I. for other timepoint groups. After incubation,

462 the cultures were rinsed with PBS for three times and replenished with 1mL fresh culture
463 medium. Then, the cultures were subjected to freezing immediately at -80°C for the 1-
464 and 2-hours samples, or continued to grow for the other groups (4, 8, 24 and 48 hours)
465 until harvest. Finally, all frozen samples from each timepoint were thawed together and
466 the viral nucleic acid abundance was measured with SARS-CoV-2 qRT-PCR Kits,
467 targeting ORF1a, E, and N genes (Liferiver Biotech, Shanghai). Results from the first
468 two time points reflect the capacity of viral attachment or entry into the target cells, while
469 results from the latter four time points represent the viral replication dynamics.
470

471 **Cytopathic effect (CPE) evaluation**

472 Vero-E6 cell monolayers were grown and infected by different patient-derived
473 SARS-CoV-2 isolates as described in the viral infectivity assay. At 24, 48, and 72 hours
474 P.I., virus induced cytopathic effects were observed with a digital microscope (Bio-Rad)
475 and pictures were taken. No obvious CPE was observed at 24 hours P.I.. Pictures taken at
476 48 and 72 hours P.I. were evaluated first by expert opinions and then quantitated by cell
477 death ratio.
478

479 **Sequencing library construction**

480 The total RNA in each deactivated viral sample was extracted using a viral RNA mini kit
481 (Qiagen, Germany). The sequencing library was constructed using the Total RNA-Seq
482 Kit (Kapa, Switzerland) and deep-sequenced on the illumina Novaseq 6000 platform (2 x
483 151 bases; Illumina Inc., San Diego, CA) by BGI genomics.

484

485 Quantification and Statistical Analysis

486 **Statistical Analyses and visualization**

487 The majority of statistical analyses and visualizations were done in Rstudio and R (at the
488 time of writing, 1.0143 for Rstudio and 3.4.0 for R), with necessary aid from customized
489 python scripts (2.7.4) and shell scripts (Linux). The primary R packages are mostly
490 maintained by the Bioconductor project (https://www.bioconductor.org/, along with all
491 their dependencies). The essential ones used are ggplot2 (2.2.1), reshape2 (1.4.3),
492 RColorBrewer (1.1-2), scales (0.5.0), corrplot (0.84), Hmisc (4.1-1), ggrepel (0.7.0),
493 cluster (2.0.6), factoextra (1.0.5), plyr (1.8.4), dplyr (0.7.4), psych (1.7.8), devtools
494 (1.13.4), ggpubr (0.1.6), tidyverse (1.2.1), gridExtra (2.3), ggsci (2.8), ggbeeswarm
495 (0.6.0), ggpmisc (0.2.16), colorspace (1.3-2).

496 In general, parametric statistical tests (t-test, Anova, and Pearson correlation) were
497 used when the data distribution conforms to normality distribution (such as qPCR
498 measurements), and non-parametric statistical tests (Wilcoxon test, Kruskal-Wallis, and
499 Spearman correlation) were used when datasets do not conform to the normality
500 assumption. We adjust the p values using the Benjamini & Hochberg (BH) method
501 (Benjamini and Yekutieli, 2001) to control for False Discovery Rate (FDR), when
502 multiple comparisons are concerned, including p value matrix constructed when
503 calculating correlations matrix among different features or samples.
504 The 3D structure of the S protein was visualized and downloaded from
505 https://www.rcsb.org/3d-view/6VSB/1.
506

507 **Sequence data processing, de novo assembling, and mutation identifications**

508 Sequencing data was generated from Novaseq 6000 and first filtered of low quality and
509 high barcode contamination by Soapnuke and then mapped to 43 complete genome
510 references of 2019-nCoV (SARS-CoV-2) by BWA-MEM (Li and Durbin, 2009).
511 References of SARS-CoV-2 were downloading from NCBI on date February 28th, 2020.
512 Further, mapping reads that longer than 100nt were extracted for de novo assemby by

513 SPAdes (Bankevich et al., 2012) (v3.1.3) using an iterative short-read genome assembly
514 module for pair-end reads. K-values were selected automatically at 33nt, 55nt and 77nt
515 for these samples. After assembling, contigs was blasted to nt database (20190301) to
516 confirm their origins, and only contigs belonging to coronavirus were retained for base
517 correction. Next, filtering reads of each sample were mapped back to retained assembled
518 contigs and bam-readcount was applied (--min-mapping-quality=5, other parameter was
519 set default) to calculate the base frequency of every post of each assemble contigs.
520 Meanwhile, Haplotypecaller of gatk was applied to call snp/indel based on the assembled
521 contigs with reads quality higher than 20. Finally, bam files were inspected in igv
522 manually to verify each mutation based on the number of reads mapped, the balance
523 between reads mapped to plus and minus strands of the reference genome, and the
524 relative positions of the mutations on these reads.
525

526 **Phylogenetic analysis**

527 We acquired 725 high quality and high coverage SARS-CoV-2 genomes from GISAID
528 (downloaded on 3/21/2020), including the Yunnan RaTG13 viral strain and the
529 Guangdong pangolin viral strain as the outgroup. We aligned the 736 genomic sequences

530 with MAFFT (Katoh and Standley, 2013) with options --thread 16 --globalpair
531 --maxiterate 1000 and trimmed the full-length alignment with trimAL (Capella-Gutiérrez
532 et al., 2009) using the -automated1 option to remove any spurious parts of the alignment,
533 which could introduce noise to the phylogenetic analysis process. We used iqtree
534 (Nguyen et al., 2015) with options -bb 1000 -alrt 1000 -nt 64 -asr to construct a
535 1000-times bootstrapped maximum-likelihood phylogenic tree of the 736 viral sequences
536 based on 835 parsimony informative sites. The resulting phylogenetic tree was imported
537 in iTOL and visualized (Letunic and Bork, 2011). We conducted Tajima's test of
538 neutrality based on the constructed alignment of viral sequences using MEGA 7 (Kumar
539 et al., 2016).
540

541 **Data and Software Availability**

542 The full-genome sequences of the 11 viral isolates have been deposited to the GISAID
543 collection with the following IDs: EPI_ISL_415709, EPI_ISL_416042, EPI_ISL_416044,
544 EPI_ISL_416046, EPI_ISL_415711, EPI_ISL_416047, EPI_ISL_416425,
545 EPI_ISL_416473, EPI_ISL_416474, EPI_ISL_418990, and EPI_ISL_418991.

546 ## Supplementary Figure Legends

547 **Table S1.** A summary of the sequencing statistics of the 11 viral isolates involved in the
548 study, Related to Figure 1. Note that ZJU_10 and ZJU_11 were sequenced in a different
549 batch.

550 **Fig. S1.** A summary of the nucleotide mutations that lead to the S247R mutations
551 observed in the 11 patient-derived isolates, Related to Figure 1. Note that some of the
552 mutations are in the form of minor alleles. Images were produced by IGV.

553 **Fig. S2.** A summary of additional mutations in the S gene and the tri-nucleotide mutation,
554 Related to Figure 1. Note that some of the mutations are in the form of minor alleles.
555 Images were produced by IGV.

556 **Fig. S3.** Phylogenetic analyses produced from GISAID using time (top) or number of
557 mutations (bottom) as the branch length, Related to Figure 2. Note that all three major
558 clusters described in the study are labeled accordingly. The major distinction is that the
559 ORF8-L84S clade is not monophyletic in our more computationally intensive and
560 bootstrapping-supported approach.

561 **Fig. S4.** The characterizations of the 11 viral isolates, Related to Figure 2 and Figure 4.
562 (A) A representative TEM picture of the isolated SAR-CoV-2 viral particles, arrows
563 indicate the iconic "crown" consisted of S proteins (Spike). (B) Time-series plots of the
564 C_t values (corresponding to the multiplicative inverse of viral load) of the SAR-CoV-2 E
565 gene (top) and N gene (bottom) over the course of infectivity assay. Each viral isolate
566 plus the negative control "C" was color-coded accordingly. P-values were calculated
567 using the ANOVA method to compare the means of all 11 viral isolates at each time
568 point, excluding the negative control "C". (C) Time-series plots of the C_t values of the
569 SAR-CoV-2 E gene (left) and N gene (right) for each of the 11 patient-derived viral
570 isolates. P-values were calculated between consecutive time points using the t-test and
571 adjusted p-values are shown.

572 **Fig. S5.** Significant variations were observed in viral load and viral CPE among the 11
573 patient-derived isolates, Related to Figure 4. (A) Significant variations in viral load can
574 be observed based on E gene (left) and N gene (right). (B) CPE at 48h and 72h P.I. as
575 evaluated by an expert's opinions. (C) CPE at 48h and 72h P.I. evaluated by quantitively
576 calculating the cell death ratio (ratio.dead) for 1-3 images per viral isolate. The results

577 from (B) and (C) are highly correlated ($R > 0.89$, $p < 0.001$). (D) Representative images
578 used for CPE evaluation, arrows indicate cells facing immediate death. Scale bars, 100
579 μm.

580 **Fig. S6.** The alignment of ACE2 protein sequences from human (Homo), Chimpanzee,
581 and green monkey (from which the Vero-E6 cell line was derived), Related to Figure 2.
582 Note that overall the ACE2 proteins are highly similar to each other. The alignment and
583 image were produced by Jalview.

584 **Fig. S7.** The 3D structure of the S-protein with the S247R overlay, Related to Figure 1.
585 The top (A), bottom (B), side (C), and close-up view (D) were provided. Note that the
586 actual position of S247 was not determined in the original structure, hence a small red arc
587 was in place to represent to the potential flexible loop conformation for (C) and (D). Also
588 note that the protein complex is trimeric, but only one of the three mutations was labeled.
589 The 3D structure of the S protein was visualized and downloaded from
590 https://www.rcsb.org/3d-view/6VSB/1.

591 **Fig. S8.** The trinucleotide mutation (G28881A, G28882A, and G28883C) was identified
592 in the GISAID dataset and is the founding mutation for a large cluster of viral isolates
593 within the S-D614G group (European clade), Related to Figure 1.

594 **Author Contributions**

595 M.Z., C.J., N.W., and L.L conceived and supervised the study. H.Y. and X.L. performed
596 all the experiments, with help from K.X., Y.C., L.C., F.L., Z.W., H.W., and C. Jin. C.J.,
597 M.Z., and Q.C. performed all the data analyses. C.J., Q.C., H.Y., and M.Z. drafted and
598 revised the manuscript with input from all authors.

599 **Acknowledgments**

600 We gratefully acknowledge Drs. X. Zhu, L. Xiang, J. Jensen, and M. Lynch for their
601 helpful discussions. We thank Dr. V. Billing for her help on improving the manuscript.

602 **Funding**

603 This work was supported by funds from Major Project of Zhejiang Provincial Science
604 and Technology Department #2020C03123, National Science and Technology Major
605 Project for the Control and Prevention of Major Infectious Diseases in China

606 (2018ZX10711001, 2018ZX10102001, 2018ZX10302206), and start-up funds from Life
607 Sciences Institute at Zhejiang University.

608 **Declaration of Interests**

609 None

610 **References**

611 Bai, Y., Yao, L., Wei, T., Tian, F., Jin, D.Y., Chen, L., and Wang, M. (2020). Presumed Asymptomatic
612 Carrier Transmission of COVID-19. JAMA - J. Am. Med. Assoc.

613 Bankevich, A., Nurk, S., Antipov, D., Gurevich, A.A., Dvorkin, M., Kulikov, A.S., Lesin, V.M., Nikolenko,
614 S.I., Pham, S., Prjibelski, A.D., et al. (2012). SPAdes: A new genome assembly algorithm and its
615 applications to single-cell sequencing. J. Comput. Biol. *19*, 455–477.

616 Bauch, C.T., Lloyd-Smith, J.O., Coffee, M.P., and Galvani, A.P. (2005). Dynamically modeling SARS and
617 other newly emerging respiratory illnesses: Past, present, and future. Epidemiology *16*, 791–801.

618 Benjamini, Y., and Yekutieli, D. (2001). The control of the false discovery rate in multiple testing under
619 dependency. Ann. Stat. *29*, 1165–1188.

620 Cao, B., Wang, Y., Wen, D., Liu, W., Wang, J., Fan, G., Ruan, L., Song, B., Cai, Y., Wei, M., et al. (2020). A
621 Trial of Lopinavir-Ritonavir in Adults Hospitalized with Severe Covid-19. N. Engl. J. Med. 1–13.

622 Capella-Gutiérrez, S., Silla-Martínez, J.M., and Gabaldón, T. (2009). trimAl: A tool for automated
623 alignment trimming in large-scale phylogenetic analyses. Bioinformatics.
624 Capobianchi, M.R., Rueca, M., Messina, F., Giombini, E., Carletti, F., Colavita, F., Castilletti, C., Lalle, E.,
625 Bordi, L., Vairo, F., et al. (2020). Molecular characterization of SARS-CoV-2 from the first case of
626 COVID-19 in Italy. Clin Microbiol Infect *0*.
627 China National Health Committee (2020). COVID-19 clinical diagnosis and management guideline issued
628 by National Health Commission of China, the 5th edition.
629 Corman, V.M., Muth, D., Niemeyer, D., and Drosten, C. (2018). Hosts and Sources of Endemic Human
630 Coronaviruses. In Advances in Virus Research, pp. 163–188.
631 van Doremalen, N., Bushmaker, T., Morris, D.H., Holbrook, M.G., Gamble, A., Williamson, B.N., Tamin,
632 A., Harcourt, J.L., Thornburg, N.J., Gerber, S.I., et al. (2020). Aerosol and Surface Stability of
633 SARS-CoV-2 as Compared with SARS-CoV-1. N. Engl. J. Med.
634 Forni, D., Cagliani, R., Clerici, M., and Sironi, M. (2017). Molecular Evolution of Human Coronavirus
635 Genomes. Trends Microbiol. *25*, 35–48.
636 Guan, W., Ni, Z., Hu, Y., Liang, W., Ou, C., He, J., Liu, L., Shan, H., Lei, C., Hui, D.S., et al. (2020).
637 Clinical characteristics of 2019 novel coronavirus infection in China. N. Engl. J. Med.
638 Hoffmann, M., Kleine-Weber, H., Schroeder, S., Krüger, N., Herrler, T., Erichsen, S., Schiergens, T.S.,

639 Herrler, G., Wu, N.-H., Nitsche, A., et al. (2020). SARS-CoV-2 Cell Entry Depends on ACE2 and
640 TMPRSS2 and Is Blocked by a Clinically Proven Protease Inhibitor. Cell 1–10.
641 Hu, Z., Song, C., Xu, C., Jin, G., Chen, Y., Xu, X., Ma, H., Chen, W., Lin, Y., Zheng, Y., et al. (2020).
642 Clinical characteristics of 24 asymptomatic infections with COVID-19 screened among close contacts in
643 Nanjing, China. Sci. China Life Sci.
644 Katoh, K., and Standley, D.M. (2013). MAFFT Multiple Sequence Alignment Software Version 7:
645 Improvements in Performance and Usability. Mol. Biol. Evol. *30*, 772–780.
646 Kumar, S., Stecher, G., and Tamura, K. (2016). MEGA7: Molecular Evolutionary Genetics Analysis
647 Version 7.0 for Bigger Datasets. Mol. Biol. Evol.
648 Lauer, S.A., Grantz, K.H., Bi, Q., Jones, F.K., Zheng, Q., Meredith, H.R., Azman, A.S., Reich, N.G., and
649 Lessler, J. (2020). The Incubation Period of Coronavirus Disease 2019 (COVID-19) From Publicly
650 Reported Confirmed Cases: Estimation and Application. Ann. Intern. Med.
651 Letunic, I., and Bork, P. (2011). Interactive Tree of Life v2: Online annotation and display of phylogenetic
652 trees made easy. Nucleic Acids Res. *39*, W475–W478.
653 Li, H., and Durbin, R. (2009). Fast and accurate short read alignment with Burrows-Wheeler transform.
654 Bioinformatics *25*, 1754–1760.
655 Lin, Q., Chiu, A.P.Y., Zhao, S., and He, D. (2018). Modeling the spread of Middle East respiratory

656 syndrome coronavirus in Saudi Arabia. Stat. Methods Med. Res. *27*, 1968–1978.

657 Lipsitch, M., Cohen, T., Cooper, B., Robins, J.M., Ma, S., James, L., Gopalakrishna, G., Chew, S.K., Tan,

658 C.C., Samore, M.H., et al. (2003). Transmission dynamics and control of severe acute respiratory syndrome.

659 Science (80-.). *300*, 1966–1970.

660 Liu, Y., Gayle, A.A., Wilder-Smith, A., and Rocklöv, J. (2020). The reproductive number of COVID-19 is

661 higher compared to SARS coronavirus. J. Travel Med.

662 Lu, R., Zhao, X., Li, J., Niu, P., Yang, B., Wu, H., Wang, W., Song, H., Huang, B., Zhu, N., et al. (2020).

663 Genomic characterisation and epidemiology of 2019 novel coronavirus: implications for virus origins and

664 receptor binding. Lancet *395*, 565–574.

665 Lv, L., Li, G., Chen, J., Liang, X., and Li, Y. (2020). Comparative genomic analysis revealed specific

666 mutation pattern between human coronavirus SARS-CoV-2 and Bat-SARSr-CoV RaTG13. BioRxiv

667 2020.02.27.969006.

668 Lynch, M. (2007). The Origins of Genome Architecture.

669 Nguyen, L.T., Schmidt, H.A., Von Haeseler, A., and Minh, B.Q. (2015). IQ-TREE: A fast and effective

670 stochastic algorithm for estimating maximum-likelihood phylogenies. Mol. Biol. Evol.

671 Ou, J., Zhou, Z., Zhang, J., Lan, W., Zhao, S., Wu, J., Seto, D., Zhang, G., and Zhang, Q. (2020). RBD

672 mutations from circulating SARS-CoV-2 strains enhance the structure stability and infectivity of the spike

673 protein. BioRxiv 2020.03.15.991844.

674 Renzette, N., Pfeifer, S.P., Matuszewski, S., Kowalik, T.F., and Jensen, J.D. (2017). On the Analysis of

675 Intrahost and Interhost Viral Populations: Human Cytomegalovirus as a Case Study of Pitfalls and

676 Expectations. J. Virol. *91*, e01976-16.

677 Schneider, M., Ackermann, K., Stuart, M., Wex, C., Protzer, U., Schätzl, H.M., and Gilch, S. (2012). Severe

678 Acute Respiratory Syndrome Coronavirus Replication Is Severely Impaired by MG132 due to

679 Proteasome-Independent Inhibition of M-Calpain. J. Virol. *86*, 10112–10122.

680 Tajima, F. (1989). Statistical method for testing the neutral mutation hypothesis by DNA polymorphism.

681 Tortorici, M.A., and Veesler, D. (2019). Structural insights into coronavirus entry. In Advances in Virus

682 Research, pp. 93–116.

683 Varia, M., Wilson, S., Sarwal, S., McGeer, A., Gournis, E., Galanis, E., and Henry, B. (2003). Investigation

684 of a nosocomial outbreak of severe acute respiratory syndrome (SARS) in Toronto, Canada. Cmaj *169*,

685 285–292.

686 Virlogeux, V., Fang, V.J., Park, M., Wu, J.T., and Cowling, B.J. (2016). Comparison of incubation period

687 distribution of human infections with MERS-CoV in South Korea and Saudi Arabia. Sci. Rep. *6*.

688 Walls, A.C., Park, Y.-J., Tortorici, M.A., Wall, A., McGuire, A.T., and Veesler, D. (2020). Structure,

689 Function, and Antigenicity of the SARS-CoV-2 Spike Glycoprotein. Cell.

690 Wang, Z., and Xu, X. (2020). scRNA-seq profiling of human testes reveals the presence of ACE2 receptor,
691 a target for SARS-CoV-2 infection, in spermatogonia, Leydig and Sertoli cells. Viruses 1–16.
692 Wang, C., Li, W., Drabek, D., Okba, N.M.A., Haperen, R. van, Osterhaus, A.D.M.E., Kuppeveld, F.J.M.
693 van, Haagmans, B.L., Grosveld, F., and Bosch, B.-J. (2020). A human monoclonal 1 antibody blocking
694 SARS-CoV-2 infection. BioRxiv 2020.03.11.987958.
695 Woelfel, R., Corman, V.M., Guggemos, W., Seilmaier, M., Zange, S., Mueller, M.A., Niemeyer, D., Vollmar,
696 P., Rothe, C., Hoelscher, M., et al. (2020). Clinical presentation and virological assessment of hospitalized
697 cases of coronavirus disease 2019 in a travel-associated transmission cluster. MedRxiv
698 2020.03.05.20030502.
699 Wu, F., Zhao, S., Yu, B., Chen, Y.M., Wang, W., Song, Z.G., Hu, Y., Tao, Z.W., Tian, J.H., Pei, Y.Y., et al.
700 (2020). A new coronavirus associated with human respiratory disease in China. Nature *579*, 265–269.
701 Xiao, F., Tang, M., Zheng, X., Liu, Y., Li, X., and Shan, H. (2020). Evidence for gastrointestinal infection
702 of SARS-CoV-2. Gastroenterology.
703 Yu, W.-B. (2020). Decoding evolution and transmissions of novel pneumonia coronavirus (SARS-CoV-2)
704 using the whole genomic data Comparative analyses of the chloroplast genome in carnivorous plants View
705 project. ChinaXriv.
706 Zhao, Y., Zhao, Z., Wang, Y., Zhou, Y., Ma, Y., and Zuo, W. (2020). Single-cell RNA expression profiling

707 of ACE2, the putative receptor of Wuhan 2019-nCov. BioRxiv 2020.01.26.919985.

708 Zhou, P., Yang, X. Lou, Wang, X.G., Hu, B., Zhang, L., Zhang, W., Si, H.R., Zhu, Y., Li, B., Huang, C.L.,

709 et al. (2020). A pneumonia outbreak associated with a new coronavirus of probable bat origin. Nature *579*,

710 270–273.

711 Zhu, N., Zhang, D., Wang, W., Li, X., Yang, B., Song, J., Zhao, X., Huang, B., Shi, W., Lu, R., et al. (2020).

712 A novel coronavirus from patients with pneumonia in China, 2019. N. Engl. J. Med. *382*, 727–733.

713

ID	Raw reads	Clean reads	Raw bases(G)	Clean bases(G)	coverage	Clean rate	Error_rate_fq 1	Error_rate_fq 2
ZJU_1	239,755,367	227,931,734	71.93	63.96	2,138,916	88.92%	0.04%	0.04%
ZJU_2	211,974,282	195,211,677	63.59	53.28	1,781,761	83.78%	0.04%	0.04%
ZJU_3	421,726,717	378,718,257	126.52	103.91	3,474,902	82.13%	0.04%	0.04%
ZJU_4	485,306,221	434,439,201	145.59	118.99	3,979,199	81.73%	0.04%	0.04%
ZJU_5	232,311,525	205,222,721	69.69	56.11	1,876,400	80.52%	0.04%	0.04%
ZJU_6	342,183,998	273,708,578	102.66	70.92	2,371,668	69.09%	0.04%	0.04%
ZJU_7	227,769,540	191,916,976	68.33	52.18	1,744,975	76.37%	0.04%	0.05%
ZJU_8	355,648,629	331,651,060	106.69	90.7	3,033,140	85.01%	0.04%	0.04%
ZJU_9	287,524,792	260,634,803	86.26	72.7	2,431,194	84.28%	0.04%	0.04%
ZJU_10	136,595,606	101,832,137	40.98	28.24	944,387	68.91%	0.02%	0.03%
ZJU_11	121,791,338	96,729,474	36.54	27.76	928,335	75.98%	0.02%	0.03%
Average	278,417,092	245,272,420	83.53	67.16	2,245,898	79.70%	0.04%	0.04%

Table S1. A summary of the sequencing statistics of the 11 viral isolates involved in the study. Note that ZJU_10 and ZJU_11 were sequenced in a different batch.

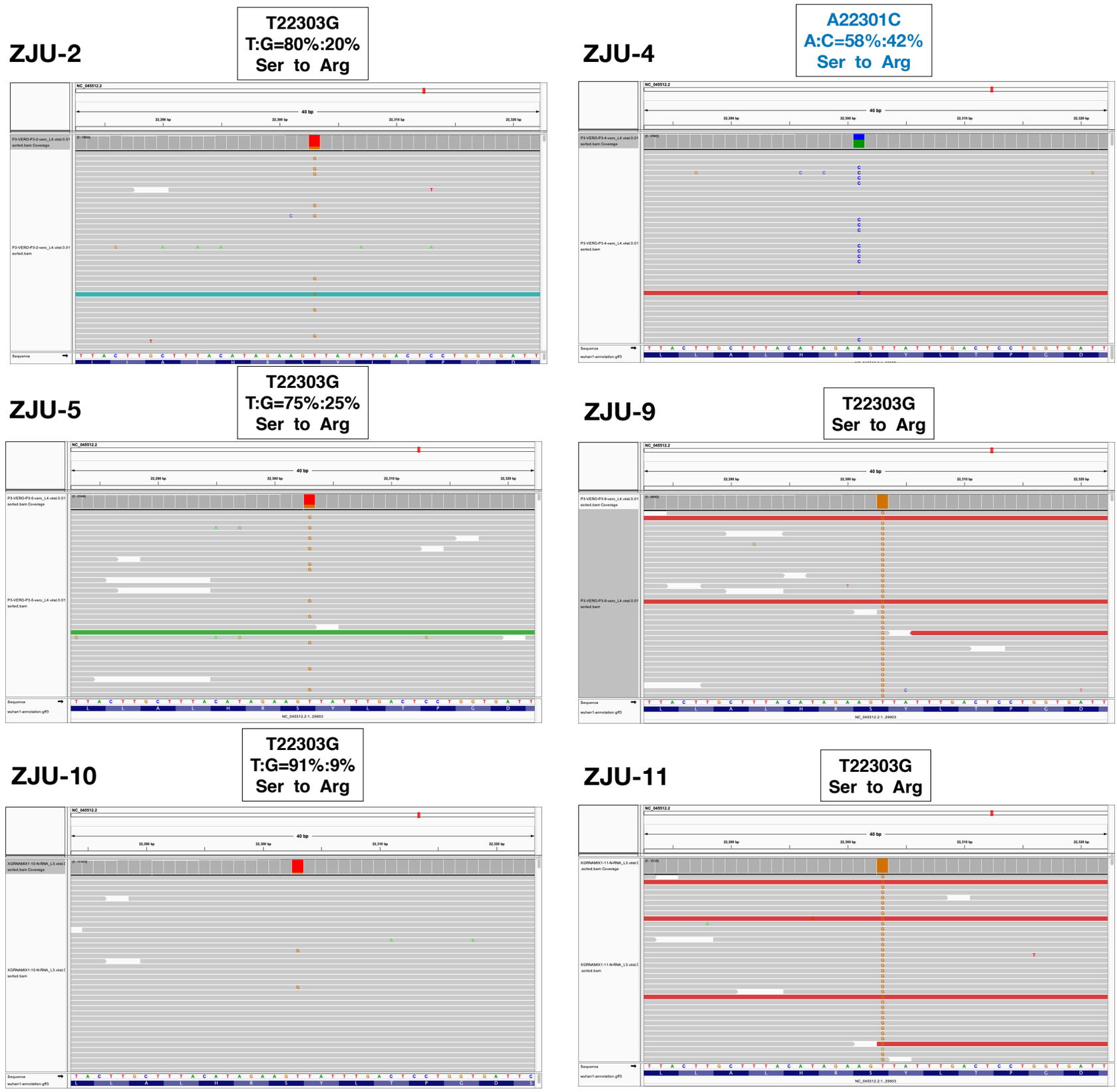

Fig. S1. A summary of the nucleotide mutations that lead to the S247R mutations observed in the 11 patient-derived isolates. Note that some of the mutations are in the form of minor alleles. Images were produced by IGV.

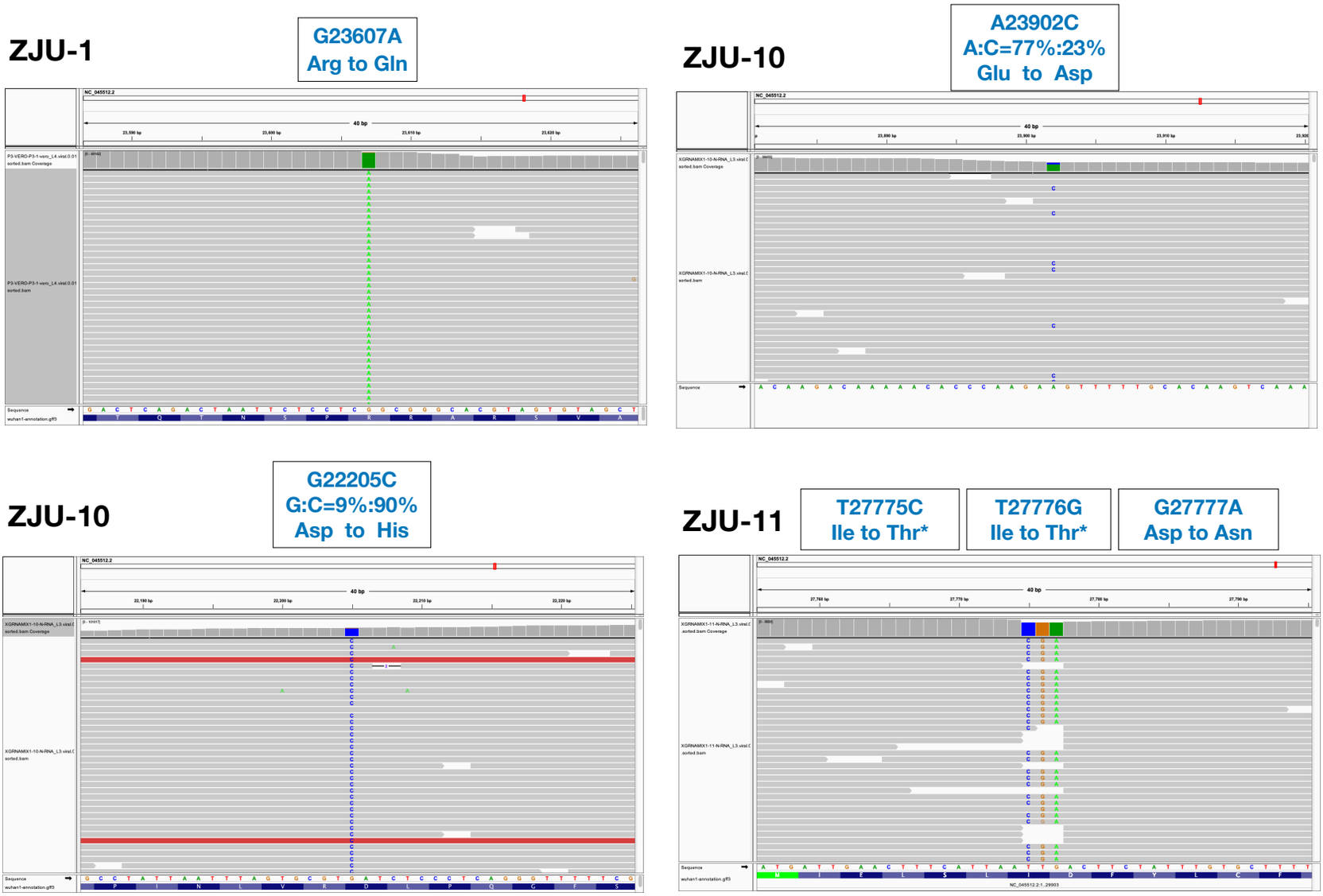

Fig. S2. A summary of additional mutations in the S gene and the tri-nucleotide mutation. Note that some of the mutations are in the form of minor alleles. Images were produced by IGV.

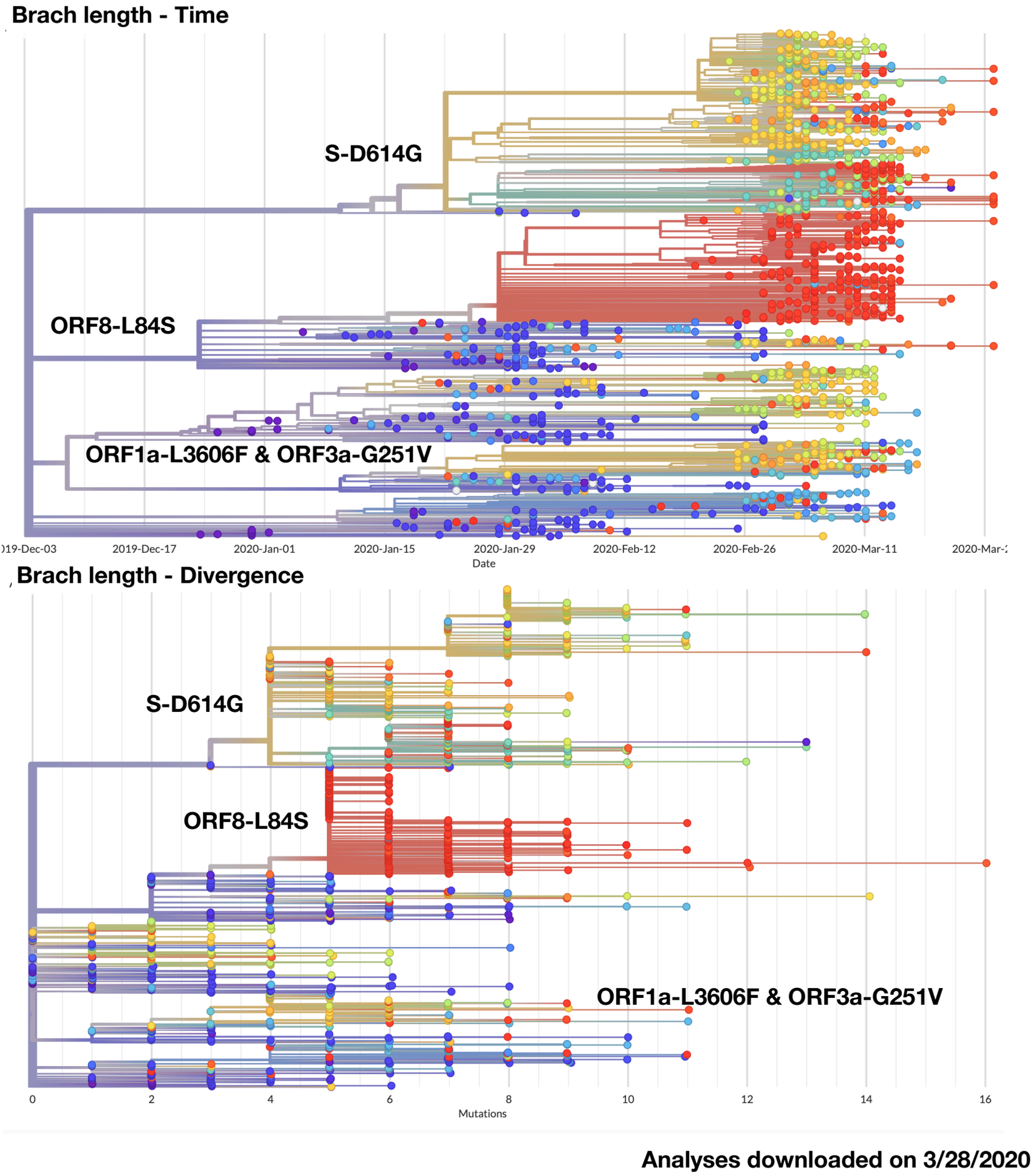

Fig. S3. Phylogenetic analyses produced from GISAID using time (top) or number of mutations (bottom) as the branch length. Note that all three major clusters described in the study are labeled accordingly. The major distinction is that the ORF8-L84S clade is not monophyletic in our more computationally intensive and bootstrapping-supported approach.

A

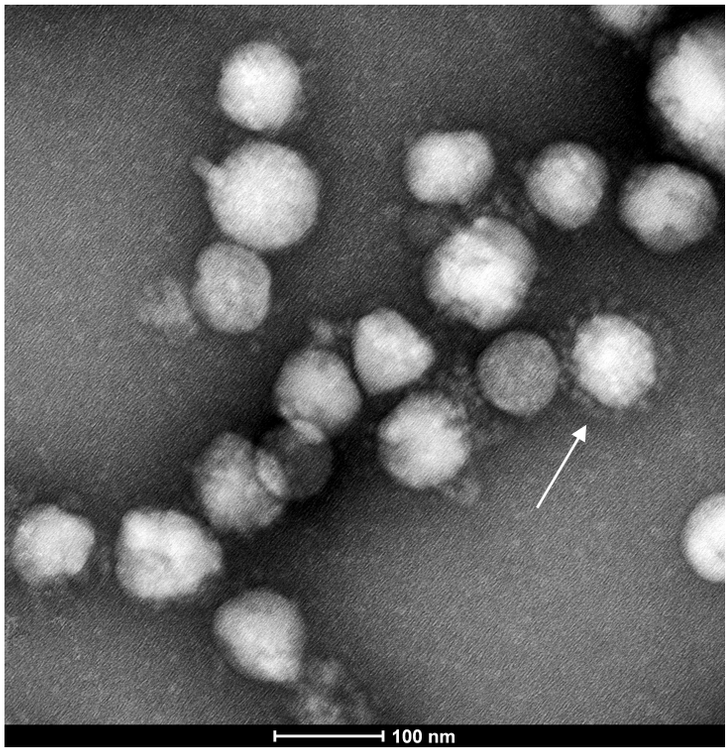
100 nm

B

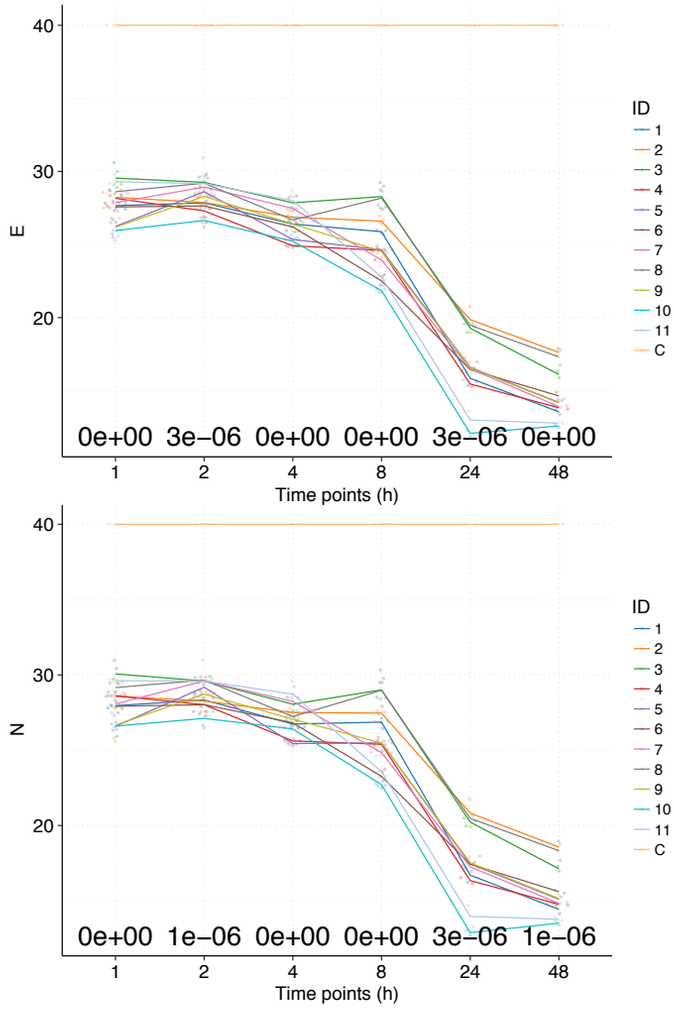
E
N
Time points (h)
ID
1
2
3
4
5
6
7
8
9
10
11
C
0e+00 3e−06 0e+00 0e+00 3e−06 0e+00
0e+00 1e−06 0e+00 0e+00 3e−06 1e−06

C

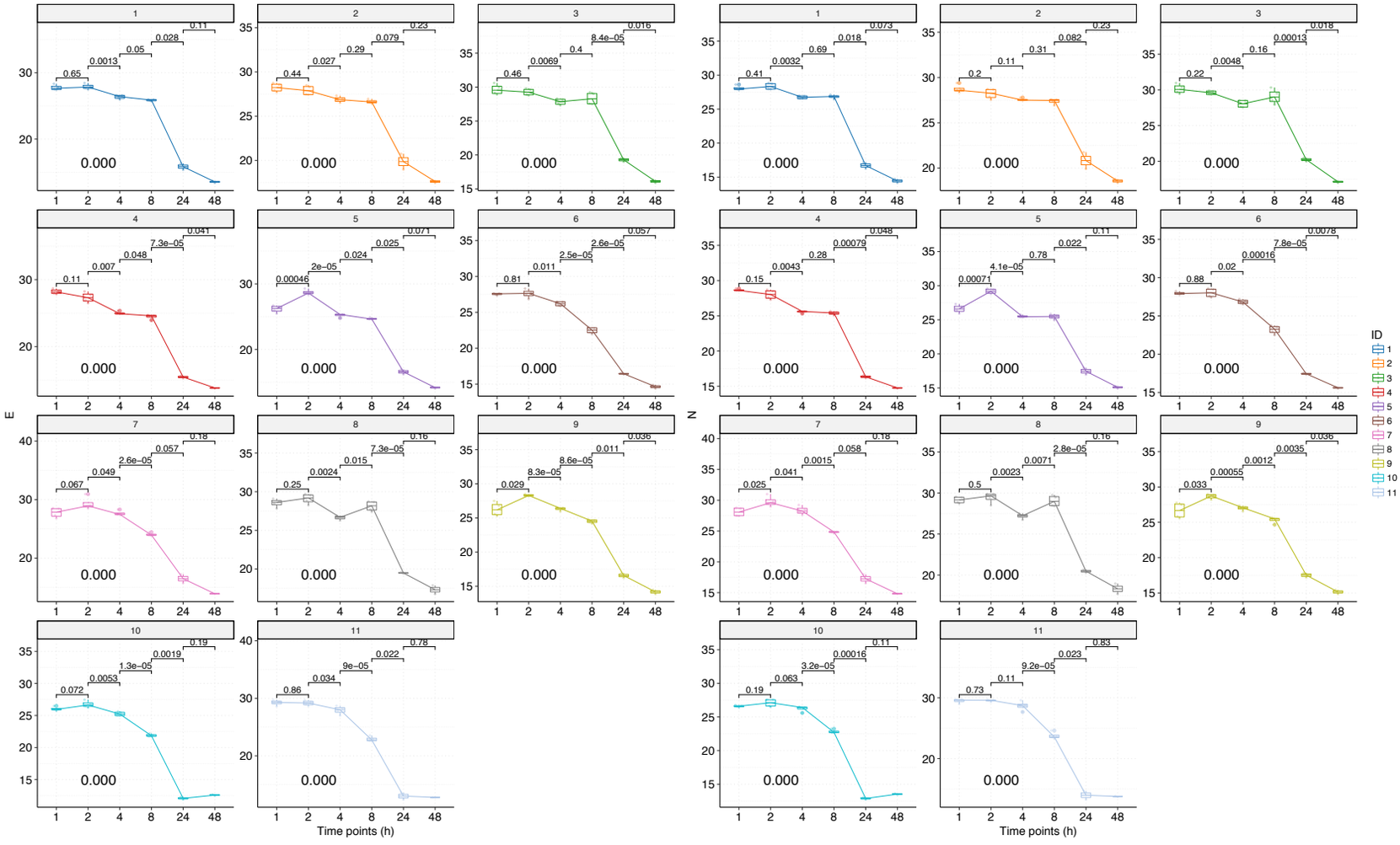
E
N
Time points (h)
ID
1
2
3
4
5
6
7
8
9
10
11

Fig. S4. The characterizations of the 11 viral isolates. (A) A representative TEM picture of the isolated SAR-CoV-2 viral particles, arrows indicate the iconic "crown" consisted of S proteins (Spike). (B) Time-series plots of the C_t values (corresponding to the multiplicative inverse of viral load) of the SAR-CoV-2 E gene (top) and N gene (bottom) over the course of infectivity assay. Each viral isolate plus the negative control "C" was color-coded accordingly. P-values were calculated using the ANOVA method to compare the means of all 11 viral isolates at each time point, excluding the negative control "C". (C) Time-series plots of the C_t values of the SAR-CoV-2 E gene (left) and N gene (right) for each of the 11 patient-derived viral isolates. P-values were calculated between consecutive time points using the t-test and adjusted p-values are shown.

A

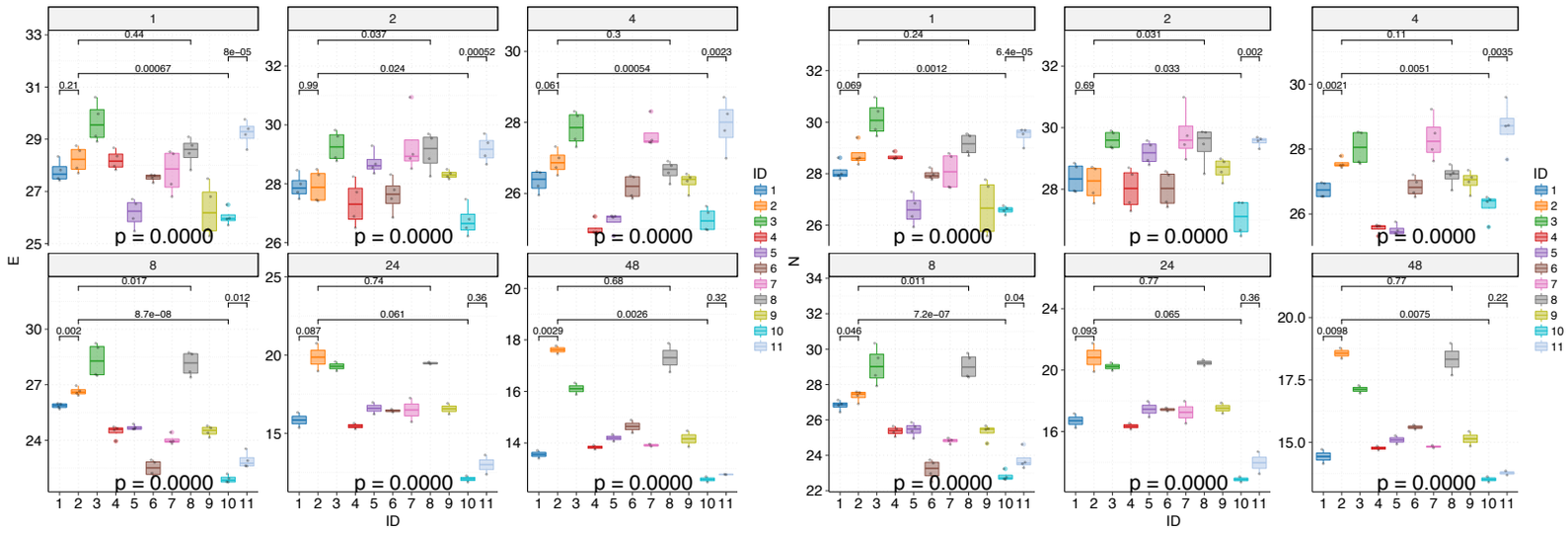

B

Viral strain ID	48 h post-infection	72 h post-infection
1	1	2
2	0	0
3	0	0.5
4	0	1
5	1	2
6	0	1.5
7	1	1
8	0	0.5
9	1.5	2.5
10	2	3
11	1	2

C

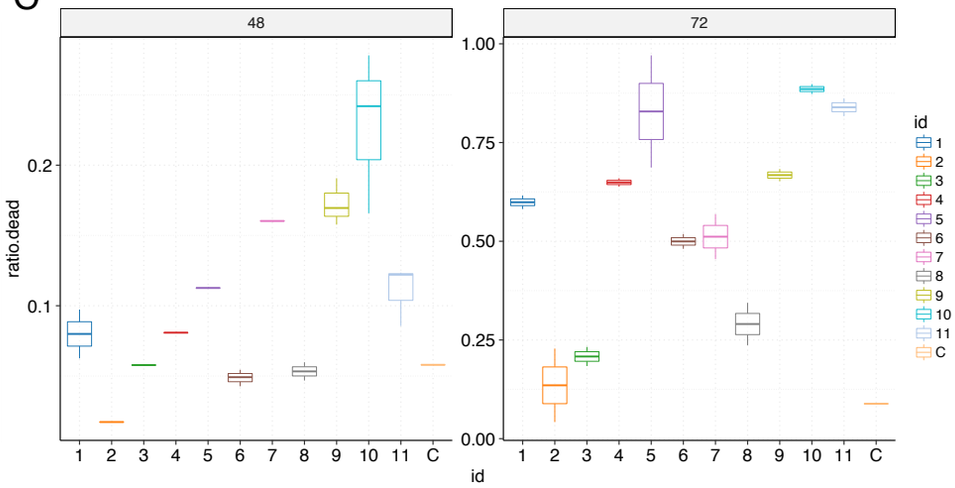

D

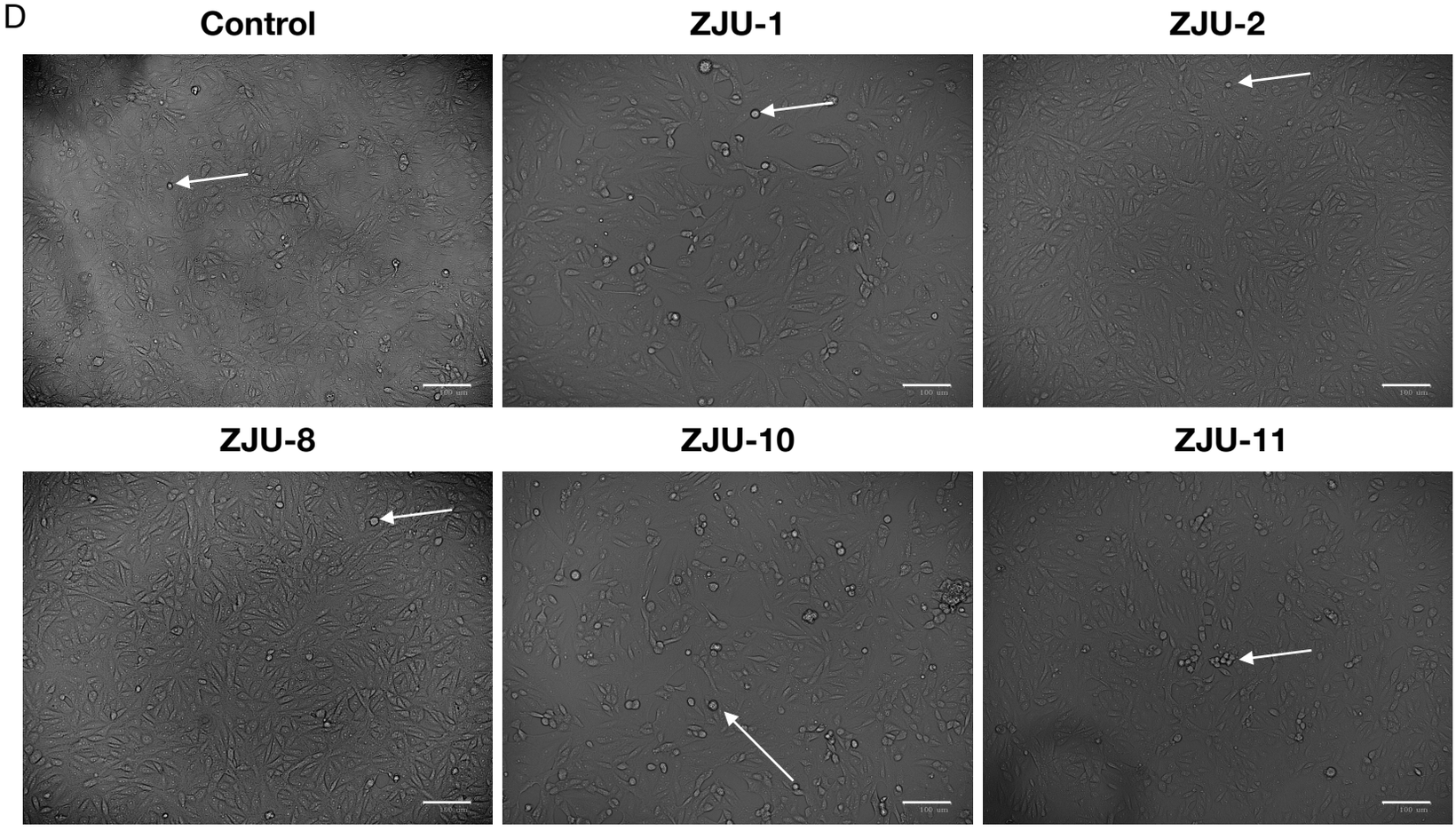

Fig. S5. Significant variations were observed in viral load and viral CPE among the 11 patient-derived isolates. (A) Significant variations in viral load can be observed based on E gene (left) and N gene (right). (B) CPE at 48h and 72h P.I. as evaluated by an expert's opinions. (C) CPE at 48h and 72h P.I. evaluated by quantitively calculating the cell death ratio (ratio.dead) for 1-3 images per viral isolate. The results from (B) and (C) are highly correlated ($R > 0.89$, $p < 0.001$). (D) Representative images used for CPE evaluation, arrows indicate cells facing immediate death. Scale bars, 100 μm.

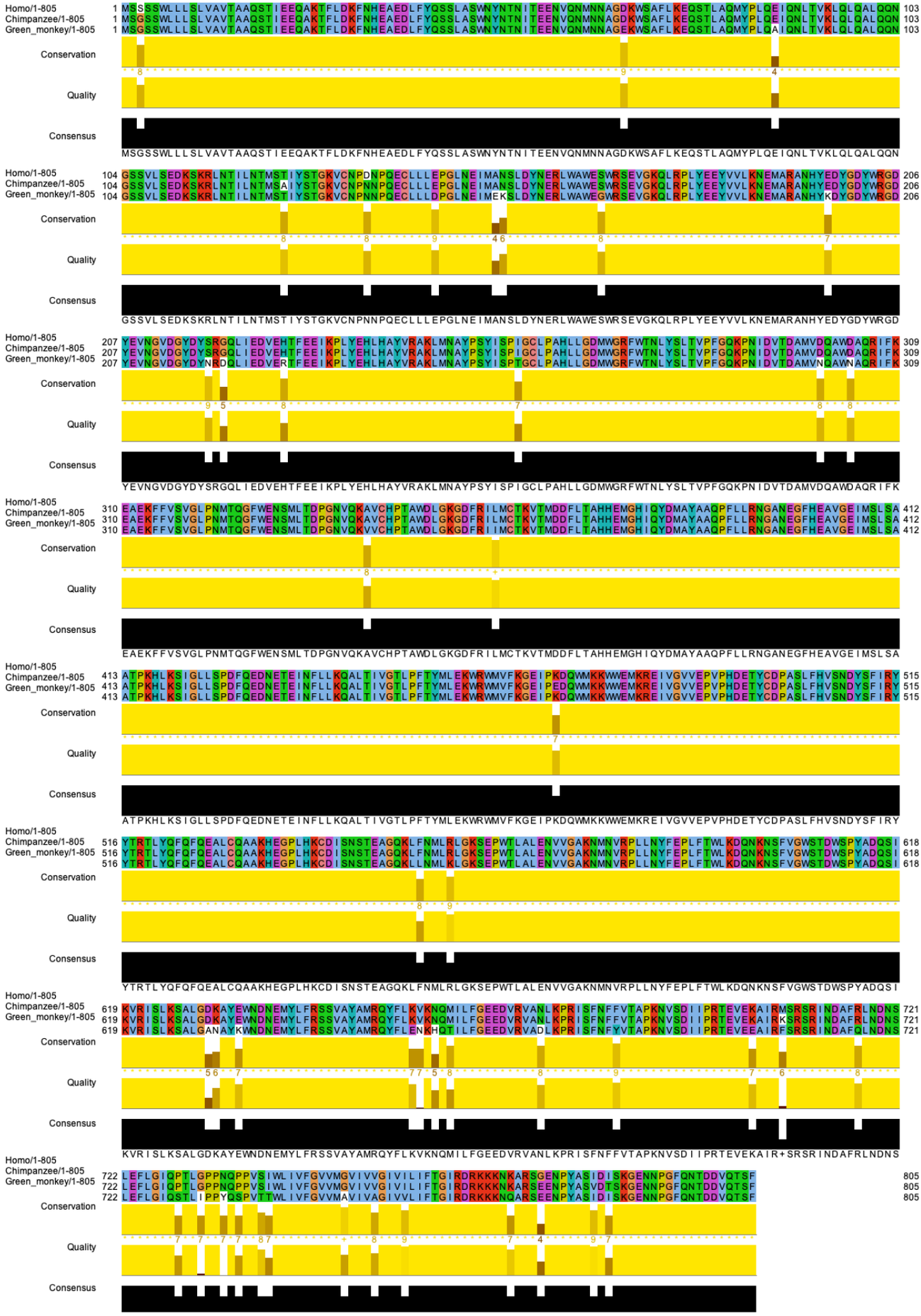

Fig. S6. The alignment of ACE2 protein sequences from human (Homo), Chimpanzee, and green monkey (from which the Vero-E6 cell line was derived). Note that overall the ACE2 proteins are highly similar to each other. The alignment and image were produced by Jalview.

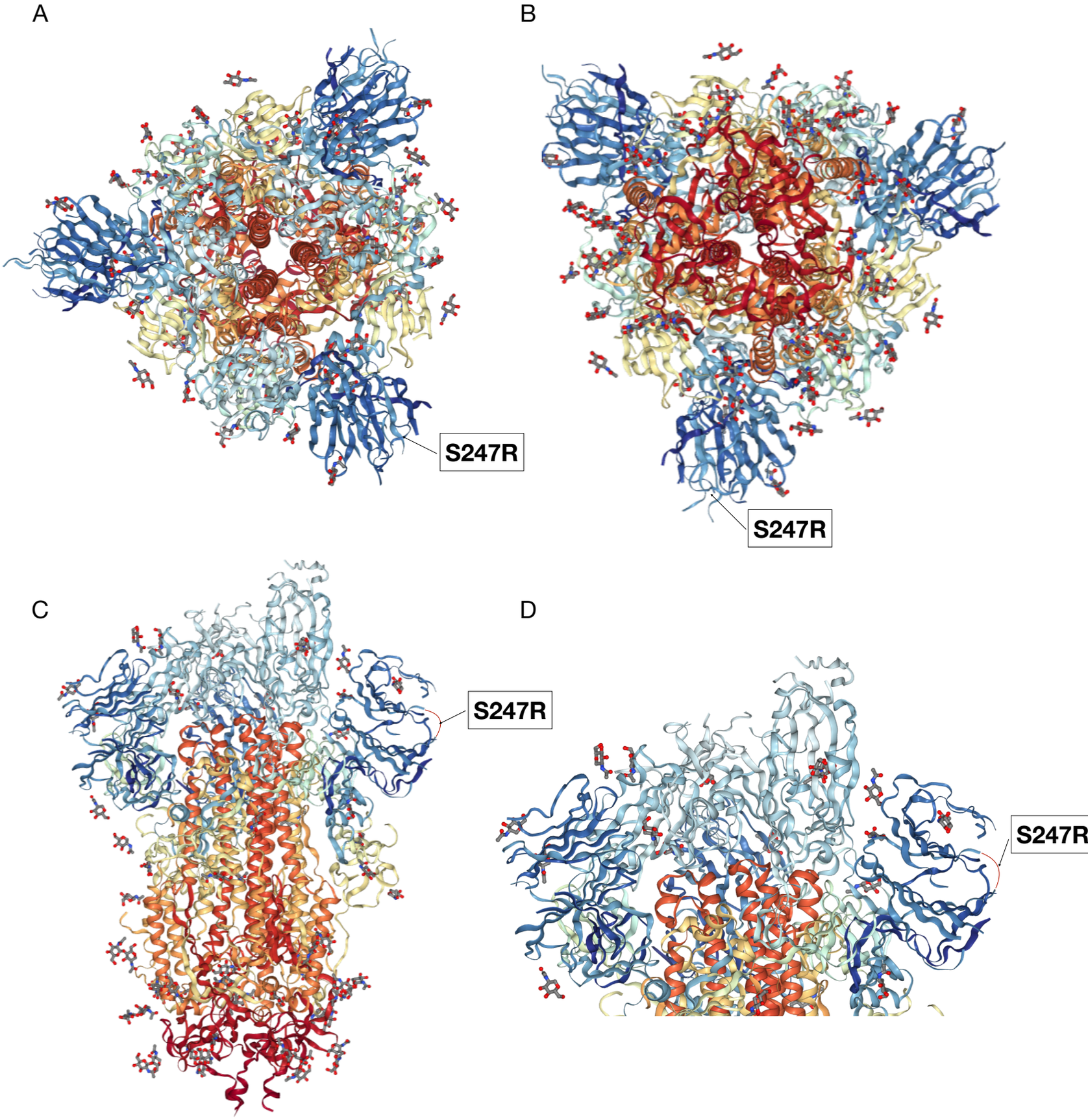

Fig. S7. The 3D structure of the S-protein with the S247R overlay. The top (A), bottom (B), side (C), and close-up view (D) were provided. Note that the actual position of S247 was not determined in the original structure, hence a small red arc was in place to represent to the potential flexible loop conformation for (C) and (D). Also note that the protein complex is trimeric, but only one of the three mutations was labeled. The 3D structure of the S protein was visualized and downloaded from https://www.rcsb.org/3d-view/6VSB/1.

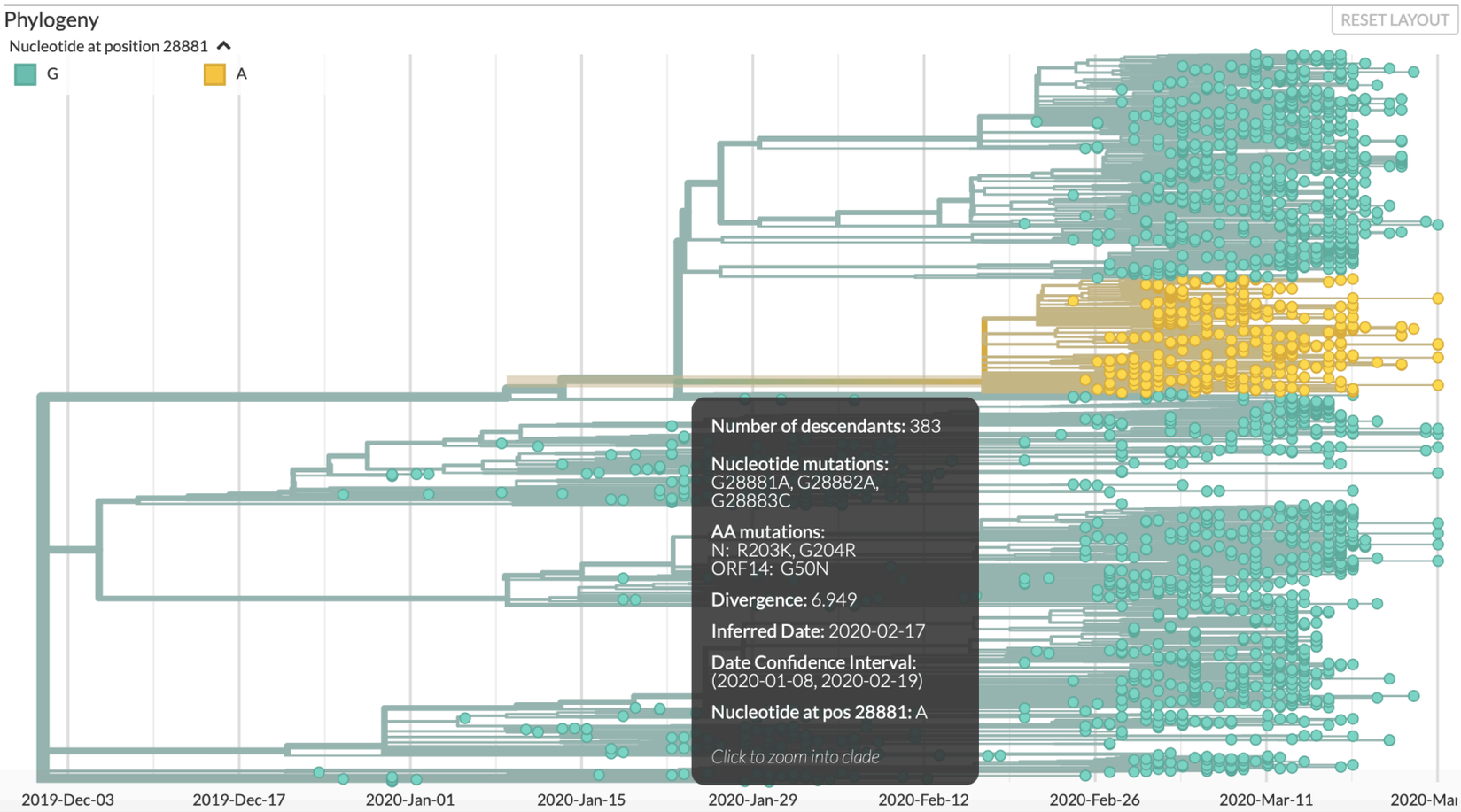

A subclade of the S-D614G group

Analyses downloaded on 3/31/2020

Fig. S8. The trinucleotide mutation (G28881A, G28882A, and G28883C) was identified in the GISAID dataset and is the founding mutation for a large cluster of viral isolates within the S-D614G group (European clade).